TURUN YLIOPISTON JULKAISUJA
ANNALES UNIVERSITATIS TURKUENSIS

SARJA - SER. A I OSA - TOM. 485
ASTRONOMICA - CHEMICA - PHYSICA - MATHEMATICA

MICROCRACKS AND VORTICES IN SUPERCONDUCTING THIN FILMS

by

Heikki Palonen

TURUN YLIOPISTO
UNIVERSITY OF TURKU
Turku 2014

From the Wihuri Physical Laboratory
Department of Physics and Astronomy
University of Turku
and
National Doctoral Programme in Nanoscience
Finland

Supervised by

Prof. Petriina Paturi
Wihuri Physical Laboratory
Dept. of Physics and Astronomy
University of Turku
Turku, Finland

Dr. Hannu Huhtinen
Wihuri Physical Laboratory
Dept. of Physics and Astronomy
University of Turku
Turku, Finland

Reviewed by

Prof. Alexey V Pan
School of Physics & Institute for
Supercond. and Elect. Materials
University of Wollongong
Northfields Avenue, Wollongong
NSW 2522
Australia

Dr. Boris Maiorov
Los Alamos Natl. Lab.
MS K764
Los Alamos
NM 87545
USA

Opponent

Prof. Pavlo Mikheenko
Department of Physics
University of Oslo
P.O. Box 1048 Blindern
0316 Oslo
Norway

The originality of this dissertation has been checked in accordance with the University of Turku quality assurance system using the Turnitin OriginalityCheck service.

ISBN 978-951-29-5689-0 (PRINT)
ISBN 978-951-29-5690-6 (PDF)
ISSN 0082-7002
Painosalama Oy – Turku, Finland 2014

Preface

Acknowledgments

This work has been carried out in Wihuri Physical Laboratory of the Department of Physics and Astronomy at University of Turku. The Jenny and Antti Wihuri Foundation, the National Doctoral Programme in Nanoscience and the Graduate School of Materials Research are acknowledged for generous financial support. Additionally, CSC — IT Centre for Science Ltd. is acknowledged for providing the necessary supercomputing resources and support.

I wish to thank Prof. A. V. Pan and Dr. B. Maiorov for carefully reviewing this dissertation and Prof. P. Mikheenko for being my opponent — it is an honor. I would like to express my sincere gratitude to Prof. P. Paturi whose brilliant supervision and guidance has kept me motivated all the way to this moment and whose efforts to arrange funding and opportunities to her students have been invaluable. Also, special thanks go to Dr. H. Huhtinen who has always been available for helpful discussions on everything, work related or not. I would like to thank Dr. J. Jäykkä for his advice, support and for all the code that he has shared for our use. Without his hard work, a large part of the work presented here would not have been possible. I am very grateful to the research group at the Wihuri Physical laboratory for the inspiring and relaxed atmosphere which has made the day at work something to look forward to.

I would like to thank my parents for granting me the freedom to pursue my interest in science and supporting me in my choice to do so. Finally, I would like to dedicate this work to my sister Elina, who is to be blamed for my choice to enrol at the University of Turku and also for the choice to begin doctoral studies.

Turku, February 2014

Heikki Palonen

Abstract

In this work, superconducting $YBa_2Cu_3O_{6+x}$ (YBCO) thin films have been studied with the experimental focus on the anisotropy of $BaZrO_3$ (BZO) doped YBCO thin films and the theoretical focus on modelling flux pinning by numerically solving Ginzburg-Landau equations. Also, the structural properties of undoped YBCO thin films grown on $NdGaO_3$ (NGO) and MgO substrates were investigated. The thin film samples were made by pulsed laser ablation on single crystal substrates.

The structural properties of the thin films were characterized by X-ray diffraction and atomic force microscope measurements. The superconducting properties were investigated with a magnetometer and also with transport measurements in pulsed magnetic field up to 30 T. Flux pinning was modelled by restricting the value of the order parameter inside the columnar pinning sites and then solving the Ginzburg-Landau equations numerically with the restrictions in place. The computations were done with a parallel code on a supercomputer.

The YBCO thin films were seen to develop microcracks when grown on NGO or MgO substrates. The microcrack formation was connected to the structure of the YBCO thin films in both cases. Additionally, the microcracks can be avoided by careful optimization of the deposition parameters and the film thickness. The BZO doping of the YBCO thin films was seen to decrease the effective electron mass anisotropy, which was seen by fitting the Blatter scaling to the angle dependence of the upper critical field.

The Ginzburg-Landau simulations were able to reproduce the measured magnetic field dependence of the critical current density for BZO doped and undoped YBCO. The simulations showed that in addition to the large density also the large size of the BZO nanorods is a key factor behind the change in the power law behaviour between BZO doped and undoped YBCO. Additionally, the Ginzburg-Landau equations were solved for type I thin films where giant vortices were seen to appear depending on the film thickness. The simulations predicted that singly quantized vortices are stable in type I films up to quite large thicknesses and that the size of the vortices increases with decreasing film thickness, in a way that is similar to the behaviour of the interaction length of Pearl vortices.

Tiivistelmä

Tässä työssä keskityttiin suprajohtavien $YBa_2Cu_3O_{6+x}$ (YBCO) ohutkalvojen tutkimiseen. Kokeellisen työn painopisteenä oli $BaZrO_3$ (BZO) lisäyksen vaikutus YBCO:n anisotropiaan. Vuon lukkiutumista ohutkalvoissa mallinnettiin ratkaisemalla numeerisesti Ginzburg-Landau -yhtälöt. Lisäksi tutkittiin $NdGaO_3$ (NGO) ja MgO alustoille kasvatettujen YBCO ohutkalvojen rakenteellisia ominaisuuksia. Ohukalvot kasvatettiin erilliskiteisille alustoille laserhöyrystyksellä.

Ohutkalvojen rakenteelliset ominaisuudet selvitettiin röntgendiffraktio- ja atomivoimamikroskooppimittauksin. Magneettiset ominaisuudet tutkittiin magnetometrilla ja resistanssimittauksin 30 T pulssitetussa magneettikentässä. Vuon lukkiutumista mallinnettiin rajoittamalla järjestysparametrin suuruutta lukkiutumiskeskuksen sisällä ja ratkaisemalla Ginzburg-Landau -yhtälöt rajoitteiden kanssa numeerisesti. Laskut suoritettiin rinnakkaislaskennalla supertietokoneella.

YBCO ohutkalvoihin havaittiin muodostuvan pieniä halkeamia, kun kalvoja kasvatettiin joko NGO tai MgO alustoille. Halkeamien muodostumisen huomattiin liittyvän YBCO ohutkalvojen rakenteeseen kummassakin tapauksessa. Lisäksi havaittiin, että halkeamien muodostumista voidaan ehkäistä kalvojen kasvatuparametrien ja paksuuden huolellisella optimoinnilla. BZO:n lisäämisen YBCO kalvoihin nähtiin laskevan elektronien efektiivisen massan anisotropiaa, mikä havaittiin sovittamalla Blatterin malli anisotropian skaalautuvuudesta mitattuun ylemmän kriittisen kentän kulmariippuvuuteen.

Ginzburg-Landau -simulaatioilla onnistuttiin toistamaan havaitut kriittisen virtatiheyden magneettikenttäriippuvuudet sekä YBCO ohutkalvoille että BZO:ta sisältäville YBCO ohutkalvoille. Simulaatioiden perusteella selvisi, että BZO:n muodostamien nanopylväiden koko vaikuttaa merkittävästi kriittisen virtatiheyden kenttäriippuvuuteen. Lisäksi Ginzburg-Landau -yhtälöt ratkaistiin tyypin I suprajohtaville ohutkalvoille, joihin nähtiin muodostuvan suurvortekseja riippuen kalvon paksuudesta. Simulaatioiden perusteella voitiin ennustaa, että yhden vuon kvantin sisältävät vorteksit ovat stabiileja tyypin I ohutkalvoissa kohtalaisen suurillakin paksuuksilla ja että vorteksien koko kasvaa kalvon ohetessa tavalla, joka on samankaltainen Pearl vorteksien vuorovaikutuspituuden kasvun kanssa.

Glossary

AC	alternating current	j_c	critical current density
AFM	atomic force microscope	L_x, L_y	x- or y-dimension of the sample
BCS	Bardeen, Cooper and Schrieffer	m	effective electron mass
BZO	$BaZrO_3$	n	fitting parameter in equation (27)
DC	direct current	n^*	Cooper pair density
FWHM	full width at half maximum	N	number of flux quanta in a vortex
IR	infrared	r	radial coordinate
LM	lattice mismatch	r_r	radius of a columnar pinning site
NGO	$NdGaO_3$	R	radius of the vortex core
PLD	pulsed laser deposition	T_dep	deposition temperature
RMS	root mean square	T_c	critical temperature
STO	$SrTiO_3$	U	fitting parameter in equation (27)
UV	ultraviolet	V	sample volume
YBCO	$YBa_2Cu_3O_{6+x}$	w	crack separation
a, b, c	lattice parameters	α	power law exponent
a_f	lattice parameter of the film	$\alpha_\mathrm{GL}, \beta_\mathrm{GL}$	Ginzburg-Landau coefficients
a_s	lattice parameter of the substrate	γ	anisotropy parameter
$\boldsymbol{A}$	vector potential	Δ	energy gap
$\boldsymbol{B}$	density of magnetic flux	Δm	opening of the hysteresis loop
B^*	accommodation field	ε	Blatter scaling function
B_irr	irreversibility field	ε_r	pinning potential
d	sample thickness	ε_0	vortex energy
e	elementary charge	θ	angle between $\boldsymbol{B}$ and a (or b)
$\boldsymbol{f}_\mathrm{p}$	pinning force density	2θ	scattering angle (XRD)
G	Gibbs free energy density	κ	Ginzburg-Landau parameter
h	Planck's constant	λ	penetration depth
$\hbar$	reduced Planck's constant	μ_0	permeability of free space
H_c	thermodynamical critical field	ξ	coherence length
H_c1	lower critical field	ψ	order parameter
H_c2	upper critical field	Ψ	tilt angle of the goniometer
H_irr	irreversibility field	$\lvert\cdot\rvert$	modulus
$\boldsymbol{j}$	current density	$\lVert\cdot\rVert$	the norm of a vector

Articles included in this thesis

This thesis is based on the experimental work carried out at the Wihuri Physical Laboratory, Department of Physics, University of Turku during the years 2010 – 2013. The thesis consists of an introductory part and of the following publications:

[**P1**] H. Palonen, H. Huhtinen and P. Paturi: *Thickness dependence of microcrack formation in $YBa_2Cu_3O_{6+x}$ thin films on $NdGaO_3$ substrates*, Thin Solid Films **519**, 8058 (2011).

[**P2**] H. Huhtinen, H. Palonen and P. Paturi: *The growth rate and temperature induced microcracks in YBCO films pulsed laser deposited on MgO substrates*, IEEE Transactions on Applied Superconductivity **23**, 7200104 (2013).

[**P3**] H. Palonen, J. Jäykkä and P. Paturi: *Modeling reduced field dependence of critical current density in $YBa_2Cu_3O_{6+x}$ films with nanorods*, Physical Review B **85**, 024510 (2012).

[**P4**] H. Palonen, H. Huhtinen, M. A. Shakhov and P. Paturi: *Electron mass anisotropy of $BaZrO_3$ doped YBCO thin films in pulsed magnetic fields up to 30 T*, Superconductor Science and Technology **26**, 045003 (2013).

[**P5**] H. Palonen, J. Jäykkä and P. Paturi: *Giant vortex states in type I superconductors simulated by Ginzburg-Landau equations*, Journal of Physics: Condensed Matter **25**, 385702 (2013).

Articles relevant to this work but not included in this thesis

[**P6**] P. Paturi, H. Palonen and H. Huhtinen: *Properties of Pr- and BZO-doped YBCO multilayers* Physics Procedia **36**, 661 (2012).

[**P7**] P. Paturi, M. Rajala, H. Palonen and H. Huhtinen: *Structural and superconducting properties of laser-deposited (110)-oriented $YBa_2Cu_3O_{7-\delta}$ thin films after in situ annealing*, IEEE Transactions on Applied Superconductivity **23**, 7200304 (2013).

[**P8**] H. Palonen, H. Huhtinen and P. Paturi: *The effect of $BaZrO_3$ nanorods on the normal state properties and on the anomaly in the even transverse resistivity in YBCO thin films*, IEEE Transactions on Applied Superconductivity **23**, 7200705 (2013).

[**P9**] P. Paturi, M. Malmivirta, H. Palonen and H. huhtinen: *The effect of BZO dopant concentration on magnetically obtained B_{irr} and B_{c2} in YBCO thin films deposited on STO substrates*, Journal of Physics: Conference series (in print).

[**P10**] M. Malmivirta, H. Palonen, H. Huhtinen and P. Paturi: *The dependence of resistively measured B_{c2} and B_{irr} on $BaZrO_3$ concentration in $YBa_2Cu_3O_{6+x}$ thin films*, Journal of Physics: Conference series (in print).

[**P11**] H. Huhtinen, H. Palonen, M. Malmivirta, R. Jha, V. P. S. Awana and P. Paturi: *The effect of $BaCeO_3$ dopant concentration on magnetically defined B_{irr} and B_{c2} in $YBa_2Cu_3O_{6+x}$ thin films deposited on $SrTiO_3$ substrates*, Journal of Physics: Conference series (in print).

[**P12**] M. Malmivirta, L. D. Yao, H. Huhtinen, H. Palonen, S. van Dijken and P. Paturi: *Three ranges of $J_{\mathrm{c}}(\theta)$ of $BaZrO_3$ doped $YBa_2Cu_3O_{7-\delta}$ thin films grown at different temperatures*, Thin Solid Films, (submitted).

Contents

Preface **iii**

Acknowledgments iii

Abstract iv

Glossary vi

Articles included in this thesis vii

1 Introduction **1**

1.1 Superconductivity 1

1.2 Ginzburg-Landau theory of superconductivity 2

1.3 Vortices and pinning 4

1.4 $YBa_2Cu_3O_{6+x}$ 7

1.5 Motivation 11

2 Experimental details **13**

2.1 Sample preparation 13

2.2 Characterization methods of structural properties 15

2.3 Characterization methods of magnetic properties 16

2.4 Solving the Ginzburg-Landau equations with flux pinning 18

3 Structural properties of YBCO thin films grown on $NdGaO_3$ and MgO **20**

3.1 Thickness dependent microcracks in YBCO films on $NdGaO_3$ 20

3.2 Microcracks in YBCO films on MgO 25

3.3 Comparison of the microcracks 28

4 Anisotropy and flux pinning in $BaZrO_3$ doped YBCO thin films **30**

4.1 The magnetic field dependence of the critical current density 30

4.2 The effect of $BaZrO_3$ doping on the anisotropy of YBCO 36

4.3 Side effects of the $BaZrO_3$ addition 40

5 Ginzburg-Landau simulations on giant vortex states in thin type I films **41**

6 Conclusions **49**

References **50**

1 Introduction

1.1 Superconductivity

A superconducting material has three distinct properties, (i) the material is perfectly conducting, (ii) the magnetic flux density vanishes inside the material, *i.e.*, the Meissner state, and (iii) there is an energy gap in the single electron states near the Fermi surface. No theory of superconductivity has been able to give a microscopic description that would cover all the known superconductors, even though it is over a hundred years since the discovery of superconductivity [1]. Although superconductivity is actually a heavily correlated many-electron state, it can often be simplified to consist of paired electrons called Cooper pairs. In 1956 Leon Cooper [2] proposed that assuming a small attractive interaction between electrons leads to the formation of Cooper pairs, a bound state of two electrons of opposite wavevectors $\boldsymbol{k}$. Soon after, Bardeen, Cooper and Schrieffer [3] (BCS) explained the basic properties of the conventional superconductors from the microscopic scale with a quantum mechanical approach. With the success of the BCS-theory it became clear that the mechanism behind the attractive interaction between the electrons is connected to the electron-phonon coupling in the conventional superconductors.

One of the predictions of the BCS-theory is the simple dependence given for critical temperature on the energy gap,

$$\Delta_0 \approx 3.52 k_{\mathrm{B}} T_{\mathrm{c}}, \tag{1}$$

where Δ_0 is the energy gap at 0 K, k_{B} is the Boltzmann constant and T_{c} is the critical temperature. Also, the BCS-theory predicts that the temperature dependence of the gap is a universal property of the conventional superconductors. Additionally, the BCS-theory predicts the jump in the heat capacity at the transition and explains the isotope effect and the Meissner state. The density of states as a function of energy E near the Fermi level has been shown to be [4]

$$D(E) \approx \begin{cases} 0, & \text{when } |E - E_{\mathrm{F}}| < \Delta, \\ \frac{D(E_{\mathrm{F}})}{\sqrt{(E-E_{\mathrm{F}})^2 - \Delta^2}}, & \text{when } |E - E_{\mathrm{F}}| > \Delta, \end{cases} \tag{2}$$

where $D(E_{\mathrm{F}})$ is the density of states at the Fermi level in the normal state. $D(E)$ of equation (2) is also shown in figure 1. The density of states is approximately constant around the Fermi level in the normal state, and in the superconducting state, the states shift from inside the gap to the edges where they accumulate into two sharp peaks.

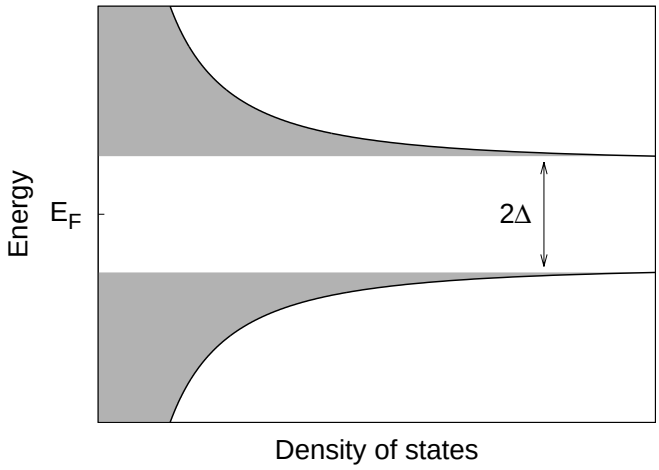

Figure 1. The density of states near the Fermi level in a superconducting material showing the gap as given by equation (2).

Due to the quantum mechanical origin of the superconductivity, the magnetic flux penetrating a hole or a normal region that is inside a superconducting region is quantized in multiples of the flux quantum

$$\Phi_0 = \frac{h}{2e}, \tag{3}$$

where h is the Planck's constant and e is the elementary charge. The quantization comes from the fact that the wavefunction has to be singly valued. Hence, the phase of the wavefunction can only be specified within modulo 2π.

1.2 Ginzburg-Landau theory of superconductivity

Superconductivity is an exceptional phenomenon in the sense that it is a quantum effect on a truly macroscopic scale. This is reflected in the fact that the properties of a superconductor can often be described with a single wavefunction, ψ, also known as the order parameter. In 1950 Ginzburg and Landau [5] developed a general thermodynamical and phenomenological treatment for superconductivity that has its roots in the Landau theory of phase transitions. The idea is to describe the extent of ordering, that is the order parameter, as proportional to the density of the superelectrons. Then expanding the Gibbs free energy density in respect to the order parameter results in the

functional [6],

$$G_{\mathrm{s}}[\psi] = G_{\mathrm{n}} + \frac{1}{V}\int \mathrm{d}^3\boldsymbol{x}\left[\frac{1}{4m}\|(-i\hbar\nabla + 2e\boldsymbol{A})\,\psi\|^2 - \boldsymbol{H}\cdot(\nabla\times\boldsymbol{A}) + \frac{1}{2\mu_0}\|\nabla\times\boldsymbol{A}\|^2 - \alpha_{\mathrm{GL}}\,|\psi|^2 + \frac{1}{2}\beta_{\mathrm{GL}}\,|\psi|^4 + \ldots\right], \quad (4)$$

where G_{s} and G_{n} are the Gibbs free energy densities for the superconducting and normal state, V is the sample volume, μ_0 is the permeability of free space, m is the effective mass of the electron, $\hbar$ is the reduced Planck's constant, $\boldsymbol{A}$ is the vector potential, $\boldsymbol{H}$ is the magnetic field strength and $\alpha_{\mathrm{GL}}, \beta_{\mathrm{GL}} \geq 0$ are the coefficients of the expansion which depend only on the temperature. The expansion is naturally valid only near the critical temperature where the order parameter is small. The first term in the integrand describes the kinetic energy related to the supercurrents in the superconductor, the next two terms are the magnetic contribution to the Gibbs and the rest of the integrand describes the potential energy of the condensate.

If the superconductor is in equilibrium, the order parameter and the vector potential have values that give a local minimum for the Gibbs free energy density. We can find the correct ψ and $\boldsymbol{A}$ by varying them and finding the minimum of the free energy. Performing the variational derivatives with respect to ψ and $\boldsymbol{A}$ gives the well-known Ginzburg-Landau equations [6],

$$\frac{1}{4m}\left(i\hbar\nabla + 2e\boldsymbol{A}\right)^2\psi - \alpha_{\mathrm{GL}}\psi + \beta_{\mathrm{GL}}\,|\psi|^2\,\psi = 0 \quad \text{and} \quad (5)$$

$$\nabla\times(\nabla\times\boldsymbol{A}) + \frac{i\hbar e}{2m}\left(\psi^*\nabla\psi - \nabla\psi^*\psi\right) + \frac{2e^2}{m}\boldsymbol{A}\,|\psi|^2 = \boldsymbol{0}. \quad (6)$$

This set of differential equations are non-linear and therefore they have to be solved numerically except for a few limiting cases. When solving the above equations it is useful to define two new characteristic lengths, the coherence length

$$\xi^2 = \frac{\hbar^2}{4m\alpha_{\mathrm{GL}}} \quad (7)$$

and the penetration depth

$$\lambda^2 = \frac{m\beta_{\mathrm{GL}}}{2e^2\mu_0\alpha_{\mathrm{GL}}}. \quad (8)$$

The coherence length describes the characteristic length scale of any changes in the order parameter while the penetration depth does the same for the magnetic field. In fact, the Ginzburg-Landau theory has only one free parameter which is called the Ginzburg-Landau parameter and is defined as

$$\kappa^2 = \frac{\lambda^2}{\xi^2} = \frac{2m^2\beta_{\mathrm{GL}}}{\mu_0 e^2\hbar^2}. \quad (9)$$

The Ginzburg-Landau parameter describes the relative importance of the energies in the Gibbs free energy. If κ is high, the energies related to the magnetic field and kinetic energy of the supercurrents are not as important as the potential energy related to the order parameter. In other words, in high-κ material the magnetic field varies only a little while the order parameter changes abruptly near the vortices.

1.3 Vortices and pinning

The Ginzburg-Landau parameter can be used to separate two interesting cases, namely the limits $\kappa \ll 1$ and $\kappa \gg 1$, respectively referred to as type I and type II superconductors. With the definitions used here, the critical value of the Ginzburg-Landau parameter separating the two types is $1/\sqrt{2}$. Elemental superconductors are typically type I and they are in the Meissner state all the way up to the critical field that is relatively low in contrast to the type II superconductors. In 1957 Abrikosov [7] showed that the high critical field of the type II superconductors is connected to the limit $\kappa \gg 1$. Between a superconducting and a normal region, there is an interface energy that is positive for low κ and negative for high-κ. When the interface energy is negative it is favourable to maximize its area. This is realized by dividing the normal regions inside the superconductor until they are so small that the magnetic field connected to the normal region is only one flux quantum. These thin cylindrical structures are called Abrikosov vortices since the the current circulates around the normal core forming a vortex.

When the energy density of the magnetic field is equal to the condensation energy, the transition from superconducting to the normal state takes place in a type I material. This field value can be derived from thermodynamical considerations to be [8]

$$H_{\mathrm{c}} = \frac{\Phi_0}{2\sqrt{2}\pi\mu_0\xi\lambda}, \tag{10}$$

where H_{c} is the thermodynamical critical field. Through the negative interface energy the formation of vortices makes it possible for the superconducting state to persist in much higher fields than the thermodynamical critical field would predict. Abrikosov also predicted that the vortices form regular triangular lattice in the superconductor which was later confirmed by Bitter decoration measurements [7, 9]. The superconductivity persists up to the upper critical field, H_{c2}, where the normal cores of the vortices start to overlap giving [6]

$$H_{\mathrm{c2}} = \frac{\Phi_0}{2\pi\mu_0\xi^2} \tag{11}$$

where $\sqrt{2}\xi$ can be interpreted as the radius of the vortex core. The Meissner state ends

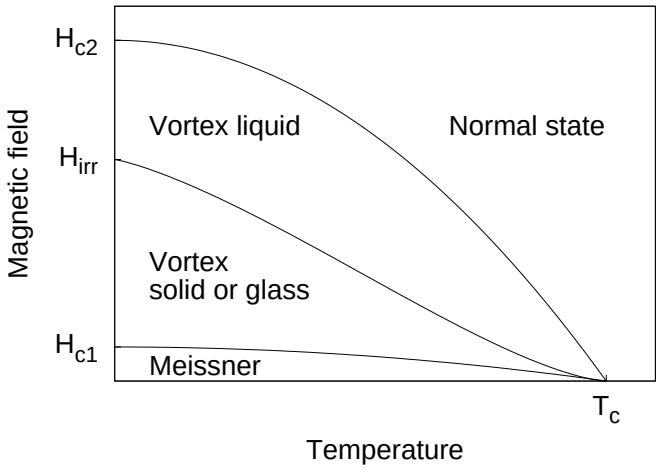

Figure 2. A simplified magnetic phase diagram of a type II superconductor showing the critical fields and the irreversibility line.

and the first vortex is formed at the lower critical field given by [6]

$$H_{\mathrm{c1}} = \frac{\ln \kappa}{2\kappa^2} H_{\mathrm{c2}}, \tag{12}$$

which is quite small compared to the upper critical field, especially in the high-κ case.

An external current pushes vortices as they experience the Lorentz force and the vortices start to flow unless there is a large enough pinning force to hold them still. The moving vortices will cause dissipation and the resistance of the superconductor is no longer zero. The system of moving vortices is called a vortex liquid. If the vortices have long or short range order the system is called a vortex solid or glass, respectively. The transition from vortex solid to the vortex liquid happens at the irreversibility field H_{irr} [6]. The magnetic phase diagram in figure 2 shows the irreversibility line and critical fields of a type II superconductor. The irreversibility field is strongly affected by the flux pinning in defects. The closer the irreversibility line is to the upper critical field the larger is the portion of the phase diagram that can be used in applications.

The force negating the Lorentz force to hold the vortex in place is called the pinning force

$$\boldsymbol{f}_{\mathrm{p}} = \boldsymbol{B} \times \boldsymbol{j}, \tag{13}$$

where $\boldsymbol{f}_{\mathrm{p}}$ is the pinning force density, $\boldsymbol{B}$ is the magnetic flux density and $\boldsymbol{j}$ is the current density. Equation (13) is valid only when $\|\boldsymbol{j}\| \leq j_{\mathrm{c}}$, where j_{c} is the critical current density. In the critical state model it is assumed that $\|\boldsymbol{j}\| = j_{\mathrm{c}}$. Since the centre of the

vortex is in the normal state, any defect that reduces the superfluid density is seen as a potential well by the vortex. Thus, the pinning force arises. The critical current density is also an extrinsic property of the material governed by the strength of the flux pinning. The pinning sites are divided into weak and strong pinning according to the strength of pinning force. Pinning is called strong if the force is strong enough to deform the vortex lattice past the elastic limit, i.e. the deformation is *plastic* [10].

Weak pinning sites are small in size when compared to the size of the vortex, so many weak pinning sites are needed to pin one vortex. The strength of this collective pinning force is determined by fluctuations instead of just simply summing up the forces of each weak pinning site [11]. The fluctuations can be, for example, in the density of the pinning sites, or the pinning sites can cause fluctuation in the critical temperature of the superconductor. In the case of collective pinning, the pinning force is calculated to each segment of the vortex separately and pinning force comes from the elastic deformation of the vortex according to the local fluctuations inside each segment [11].

In the case of a single vortex and strong columnar pinning site, an upper limit to the pinning potential can be derived within the high-κ approximation [11]

$$\varepsilon_{\mathrm{r}} = \frac{\varepsilon_0}{2} \ln\left(1 + \frac{r_{\mathrm{r}}^2}{2\xi^2}\right), \tag{14}$$

where ε_{r} is the pinning potential, r_{r} is the radius of the columnar pinning site and ε_0 is the characteristic energy of the vortex per unit length given by

$$\varepsilon_0 = \frac{\pi\hbar^2}{4\mu_0 e^2 \lambda^2}. \tag{15}$$

Basically ε_0 gives an idea how much it costs in energy if the length of vortex increases due to following a path through a pinning site instead of going as straight line through the sample.

While the idea of a single vortex pinning to a defect is relatively simple, the situation gets almost overwhelmingly complicated when the interactions with all the other vortices and all the different defect types present in any real material are put in. To be able to say something about the magnetic field dependence of j_{c} the vortex-vortex interactions must be included in the model. The magnetic field dependence can be roughly separated into three regions schematically shown in figure 3. First, at low magnetic fields, the single vortex pinning dominates and the critical current density stays constant. Then above the accommodation field the vortex-vortex interactions come into play and the critical current density decreases. The pinning in that region is called small bundle pinning because there are several vortices pinned to each pinning site. In the

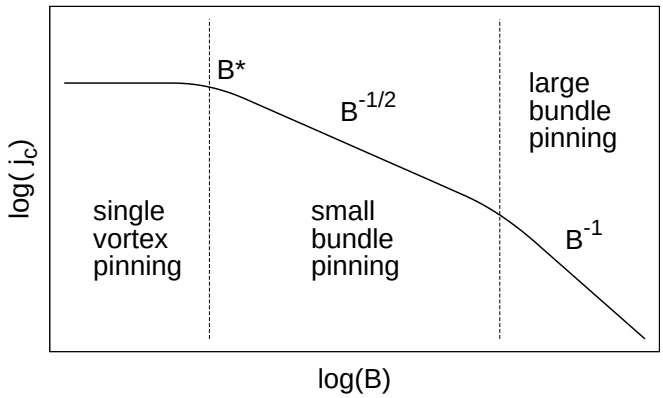

Figure 3. A simplified magnetic field dependence of the critical current density.

highest fields large bundle pinning makes the critical current density to decrease even faster [11]. In experimental context, the accommodation field B^* is defined as [12, 13]

$$\frac{j_{\mathrm{c}}(B^*)}{j_{\mathrm{c}}(0)} = 0.9, \tag{16}$$

above which the critical current density decreases according to the power law [14]

$$j_{\mathrm{c}} \propto B^{-\alpha} \quad \text{when } B > B^*, \tag{17}$$

where α has different values depending on the model. Blatter *et al.* give $\alpha = 0.5$ [10] for the small bundle pinning regime and $\alpha = 1$ [11] for the large bundle pinning while van der Beek *et al.* give $\alpha = 0.63$ [15] assuming sparse strong pinning sites.

1.4 $\mathbf{YBa_2Cu_3O_{6+x}}$

The promising cuprate $YBa_2Cu_3O_{6+x}$ (YBCO) was discovered in 1987 soon after the discovery of the first high temperature superconductor in 1986 by Bednorz and Müller [16, 17]. The critical temperature of YBCO was resistively measured to be 92 K [16] which aroused a lot of attention since it is above the boiling point of liquid nitrogen. There is still quite a lot of variation in the superconducting parameters measured from YBCO single crystals, for example, for the penetration depth λ_{ab} values ranging from 26 nm to 260 nm have been measured [6]. With the Ginzburg-Landau simulations we used 150 nm [18] for the value of the penetration depth [**P3**]. Some averages of the superconducting properties of YBCO are collected in table 1. As can be seen from the table 1, YBCO is an anisotropic high-κ superconductor with a very large upper critical field.

Table 1. Basic superconducting properties of YBCO. The coherence length and penetration depth values are averages from [18, 22–24]. The lower critical field values are averages from [18, 24–26] and the upper critical fields from [18, 27, 28]. The last column has been calculated from the other values in the table. In the case of the characteristic lengths, the a, b, or c indicate the crystalline direction or, in other cases, the direction of the magnetic field.

	nm		T		
ξ_{ab}	1.5	H_{c1}^{ab}	0.05	κ_{ab}	500
ξ_c	0.2	H_{c1}^{c}	0.18	κ_c	90
λ_{ab}	140	H_{c2}^{ab}	200	γ	6
λ_c	600	H_{c2}^{c}	60		

The atomic structures of tetragonal and orthorhombic YBCO are shown in figure 4. $YBa_2Cu_3O_{6+x}$ is tetragonal when $x < 0.35$ and orthorhombic when $x > 0.35$ [19]. The tetragonal phase is not superconducting, and in it the excess oxygen occupy the both oxygen sites in the basal plane at equal probability while in the orthorhombic phase the other site is always empty and the oxygens form chains [19]. The superconductivity is in the CuO_2 planes and the oxygen vacancies in the chains adjust the hole doping in the planes. In the orthorhombic phase there are two plateaus in the T_c as a function of the oxygen content, corresponding to the $\sim$90 K and $\sim$60 K phases. It is the ordering of the oxygen into chains and chain superlattices that is behind these plateaus [20, 21].

The layered structure of the CuO_2 planes leads to a high intrinsic anisotropy in YBCO. From the point of view of the applications the anisotropy is an unwanted property, isotropic materials are better and easier in device design and performance. The anisotropic effective electron mass is reflected in almost all the material parameters as can be seen in table 1. In the case of a high-κ superconductor, an anisotropic thermodynamic quantity can be scaled into an isotropic one by using a scaling function [29]

$$\varepsilon(\theta) = \sqrt{\sin^2\theta + \frac{1}{\gamma^2}\cos^2\theta}, \tag{18}$$

where θ is the angle between the magnetic field and the CuO_2 plane of YBCO and $\gamma^2 = m_c/m_{ab}$ is the anisotropy parameter. As can be calculated from the values in table 1, the anisotropy of YBCO varies around 6. The scaling function is applicable for many quantities but two of them are of particular interest, the upper critical field and the

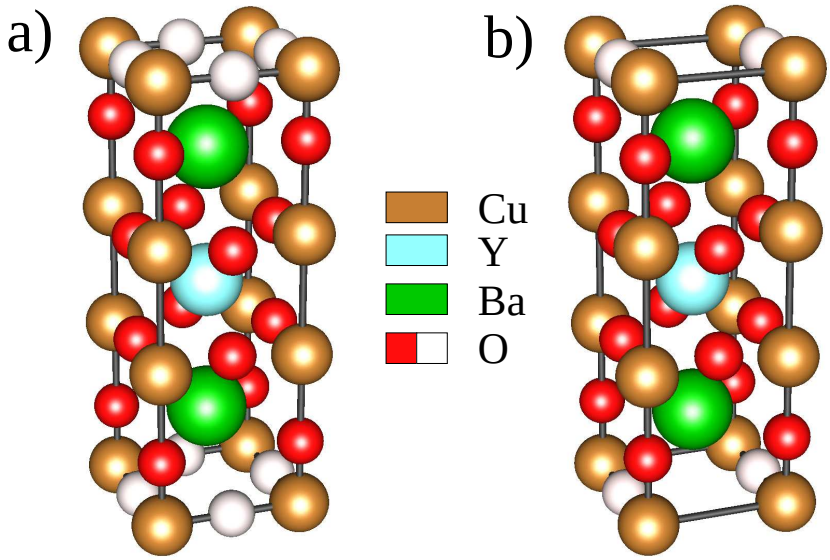

Figure 4. The unit cell of a) tetragonal and b) orthorhombic YBCO. The white spheres are oxygen sites that are only partly occupied. In the case of $YBa_2Cu_3O_6$ (tetragonal), they are all empty and with $YBa_2Cu_3O_7$ (orthorhombic) completely occupied. The phase transition takes place when the composition is near $YBa_2Cu_3O_{6.35}$.

critical current density.

The scaling (18) is often used in fitting the angle dependence of the critical current density of YBCO. The problem is that the scaling only takes the electron mass anisotropy into account while the critical current density is an extrinsic property affected by many other sources of anisotropy, like correlated pinning effects. As a result, the anisotropy parameter γ is replaced by an effective γ_{eff} which is determined by data fitting. Typically, the result is 5–7 for undoped YBCO but, if the sample has a high density of correlated or strong pinning sites, the values are much lower, in the range of 1.5–2 [30–32]. It is unclear to what extent such low γ_{eff} values are a result of lowered electron mass anisotropy or a result of correlated pinning effects. Wimbush and Long even go so far as to claim that the whole idea of fitting the scaling model to an extrinsic property, such as the critical current density, is simply nonsense [33]. On the other hand, it has also been explained that the Blatter scaling works for point-like pinning sites because they remain invariant in the scaling but not for other kinds of pinning sites [32, 34].

For the upper critical field the Blatter scaling predicts an angular dependence of the form [29]

$$H_{c2}(\theta) = \frac{H_{c2}^{H||c}}{\varepsilon(\theta)}, \tag{19}$$

where $\varepsilon(\theta)$ is the scaling function from equation (18) and $H_{c2}^{H||c}$ is the value of the upper critical field at the field out-of-plane position. As is seen in [**P4**], the angle dependence of the upper critical field follows equation (19) quite well which means that $H_{c2}^{H||ab}$ is roughly six times larger than $H_{c2}^{H||c}$. In the literature, the values measured for the anisotropy of undoped YBCO from the upper critical field range in between 5 and 9 [35–37].

A YBCO thin film has plenty of defects that can act as pinning centres. These include, for example, stacking faults, twin boundaries, dislocations, point defects and, if the film is of lesser quality, precipitates, voids and grain boundaries [38]. With linear defects like dislocations, the pinning is stronger if the vortex is aligned with the dislocation while the point defects are isotropic pinning sites. The relative size of the pinning site to the vortex is important. If the defect is small, for example, an oxygen vacancy in YBCO, the thermal smearing makes it easy for the vortex to jump from one vacancy to the next. As a result, it is not the absolute density of the oxygen vacancies but the fluctuations in it that bring about the pinning force [10]. In the case of larger pinning sites like dislocations, a large density of defects will cause a larger pinning force but the situation is made more complicated by the anisotropic nature of the linear defect. Eventually, a large defect density will suppress the superconducting properties and the density is past the optimum. If two large pinning sites, holes for example, are too close to each other, the superconductivity in between is disturbed by the vicinity of the interfaces. The ultimate theoretical limit is given by the depairing current density at which just the kinetic energy is enough to break the Cooper pairs.

The pinning landscape in YBCO can be improved by adding artificial pinning centres into the material. The methods for making artificial pinning sites include, for example, particle irradiation, substrate decoration or adding non-superconducting material. The irradiation of YBCO single crystals with protons causes uncorrelated pinning while heavy ions cause correlated, columnar pinning centres [39, 40]. The irradiation is impractical and in thin films the improvement is small [41]. Adding non-superconducting nanoparticles is a common method to incorporate artificial pinning centres. $BaZrO_3$ (BZO) and $BaSnO_3$ form columnar nanorods in pulsed laser deposited YBCO thin films [42–45] while, for example, Y_2O_3 forms isotropic nanoparticles [45, 46]. An

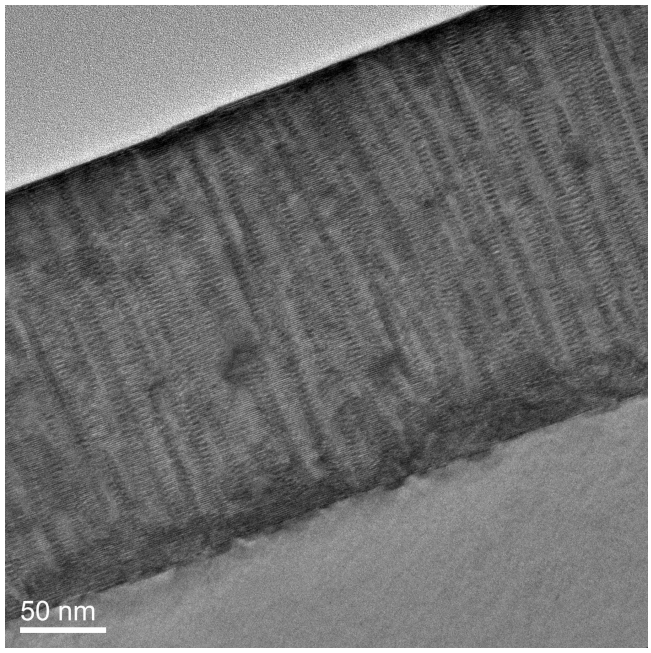

Figure 5. Transmission electron microscope image of a BZO doped YBCO thin film cross section. The BZO nanorods are visible as parallel lines aligned with the YBCO c-axis. [48]

example of the columnar structure of BZO nanorods in a pulsed laser deposited YBCO thin film is shown in figure 5. The nanorods are aligned with the YBCO c-axis and increase the critical current density considerably in high magnetic fields when the field is aligned with the nanorods [30, 47].

1.5 Motivation

After the initial optimism triggered by the discovery of the high temperature superconductivity, the research on YBCO has now become more settled and aims for perhaps a bit more realistic goals. One of the main prospects is the possibility of lossless electricity transfer at liquid nitrogen temperature which utilizes the high critical temperature of YBCO. An other aspect is based on the remarkably high upper critical field of YBCO which can be used in superconducting magnets as, for example, high field inserts working at the liquid helium temperature. The experimental research on YBCO can be divided into two categories: one focusing on the more technical side aiming for higher and higher performance numbers for large scale applications and the other is more focused on the reasons behind the numbers, studying flux pinning and material properties

more closely. Here, the latter aspect has been pursued by experimental work on the material properties of YBCO grown on ideal single crystal substrates and by theoretical simulations modelling the flux pinning in YBCO. The work is motivated by the need to improve and understand the properties and flux pinning in YBCO and by academic interest in vortex states in general.

Because of the ceramic and brittle nature of YBCO, one of the experimental challenges is to grow YBCO coatings or films that have the properties approaching that of a single crystal YBCO while avoiding the formation of grain boundaries or cracks, and all this up to a reasonable thickness. On the theoretical side, the understanding of the flux pinning is still rather limited. The basic principles are quite established but the full implications of, for example, columnar pinning sites to the superconducting properties of the material are not yet clear. The current numerical methods, computational resources and software enable a new approach to the flux pinning problem complementing the conventional analytical approach.

After the introductory parts of this thesis, the first part of the discussion will be about the microcracks forming in YBCO PLD films on MgO and $NdGaO_3$ substrates. The second part will concentrate on the effect of columnar pinning sites, $BaZrO_3$ in particular, on the superconducting properties of YBCO with the main focus on the field dependence of the critical current density and on the anisotropy of the upper critical field. The giant vortex states and type II behaviour, which appear in confined type I superconductors, will be discussed in the final part.

2 Experimental details

2.1 Sample preparation

The YBCO samples were prepared with pulsed laser deposition (PLD) which is a suitable method for making thin films of complex oxide materials that are sensitive to the composition of the atmosphere during the growth. A schematic description of the experimental setup is shown in figure 6. In short, the thin film is grown on a heated substrate by shooting at the target with a pulsed UV-laser (308 nm). The energy from the laser ejects a cone of plasma, also known as the plume, from the target. The plume is adjusted to hit the substrate and a thin film is formed.

The substrate is chosen so that its lattice parameters are close to the ones the desired target material has. In the case of YBCO, the commonly used substrates include $SrTiO_3$ (STO), MgO and $NdGaO_3$ (NGO). Of course, these single crystal substrates are not suitable for industrial scale use, where technical substrates, e.g. NiW with buffer layers, are used [38]. The lattice mismatch (LM) between the film and substrate can be described with

$$\mathrm{LM} = \frac{2(a_\mathrm{s} - a_\mathrm{f})}{a_\mathrm{s} + a_\mathrm{f}}, \tag{20}$$

where a_s and a_f are the lattice parameters of the substrate and film, respectively. The values of LM and lattice parameters for a few substrates are shown in table 2. STO and NGO are favoured as subtracted due to their low lattice mismatch, while MgO is used when a low dielectric constant of the substrate is needed, for example, in microwave applications [49].

Good quality targets are necessary in the PLD. The stoichiometry of the metal ions in the target transfers directly to the film while the oxygen is added by *in situ* heat treatments. In this work, targets made with two different methods have been used: solid state reaction targets and citrate-gel targets that are made as described in [50]. A solid state reaction target has a grainsize of several micrometers, while in the citrate-gel targets the grainsize is 50 nm or even less. In the case of BZO doped YBCO the targets were also made with the citrate-gel method. The citrate-gel method yields a fine powder because both the fuel and oxidizer are present and well mixed in the dried gel that can then be fired very rapidly. The solid state method yields coarser grained powder than the citrate-gel method because the reaction relies only on the diffusion of the reagents in the heat treatments. In this work, samples made with the solid state target are referred to as µ-films and samples made with the citrate-gel target as n-films.

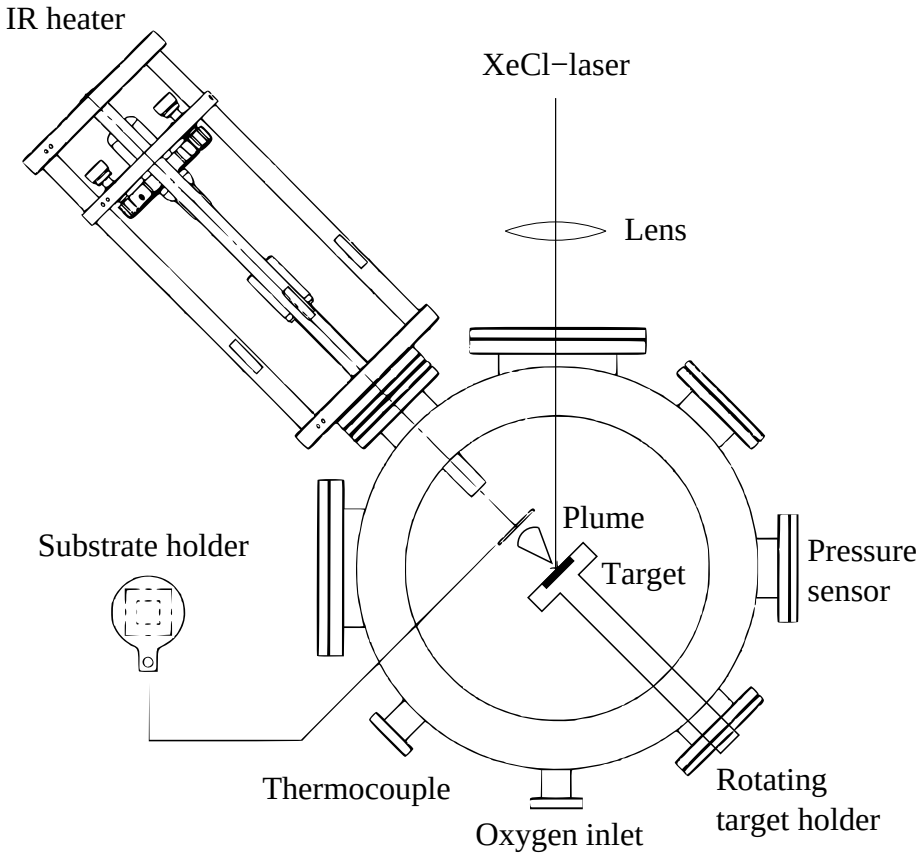

Figure 6. A schematic sketch of the PLD chamber with its key components shown.

Table 2. Lattice parameters and mismatches for the different substrates used in this work. The lattice parameter values are averages of those given in the references.

	Structure	Lattice parameters			LM*	Ref.
		a (Å)	b (Å)	c (Å)	(%)	
MgO (100)	cubic	4.212	-	-	8.9	[51, 52]
$NdGaO_3$ (001)	orthorhom.	5.430	5.500	7.711	0.2	[53–55]
$SrTiO_3$ (100)	cubic	3.902	-	-	1.2	[56, 57]
$YBa_2Cu_3O_{6.93}$	orthorhom.	3.823	3.887	11.680	-	[19]

*Compared to the average of the a and b lattice parameters of YBCO.

The sample preparation is typically done as follows. The sample is heated up to the deposition temperature (T_{dep}) that is optimal in the range from 730 °C to 770 °C and the film is grown with UV-laser pulse frequency of 5 Hz and energy of 80 mJ (1.7 J/cm^2). The optimal pressure of the flowing O_2 during the deposition is 20–40 Pa. After the deposition the sample is oxygenated in 1 atm of pure O_2 for ten minutes and then cooled down at a cooling rate of 25 °C/min. The growth rate of the film is about 1.1 Å per pulse so that a typical film of 1500 pulses is roughly 160–170 nm thick. After structural and magnetic measurements the sample preparation is continued by etching a standard four probe pattern on it by photolithography for transport measurements.

2.2 Characterization methods of structural properties

The surface structure and thickness of the YBCO films were characterized by the atomic force microscope (AFM), *Park Scientific Instruments Autoprobe CP-research system*. In short, the contact mode AFM works by sensing the repulsive part of Van der Waals force between a cantilever tip and the surface of the sample. The movement of the cantilever is recorded with a pair of photodetectors that sense the change in the reflection of a laser beam from the cantilever surface. The sample is moved under the cantilever with a 100 x 100 μm^2 scanner and an image of the sample surface is formed. The typical image sizes used were from 5 x 5 μm^2 to 50 x 50 μm^2. The images were then analyzed so that the surface root mean square (RMS) roughness and, after the etching, the film thickness could be measured.

The structure of the YBCO films was further investigated with x-ray diffraction (XRD). When a material is illuminated with x-rays, each atom in the lattice acts as a scattering centre. Due to the symmetry of the lattice the scattered photons interfere and interference maxima form according to the Bragg's law [58]. XRD was used to verify the purity of the YBCO thin films. Additionally, XRD was used to get information about the growth direction, twin boundaries, strain and mosaic spread in the films.

The measurements were done with a *Philips X'pert Pro* diffractometer with Cu K_α radiation filtered with Ni in the symmetric Bragg-Brentano $\theta - 2\theta$ configuration. Except for the rocking curves where the angle 2θ between the incident and collected beam is held fixed and the sample is tilted non-symmetrically. In addition to a general 2θ scan a more detailed measurement was made for the YBCO (005) ($2\theta = 38.6°$, $\Psi = 0°$), (102) ($2\theta = 27.8°$, $\Psi = 56°, 31°$) and (122)/(212) ($2\theta = 55.5°$, $\Psi = 73°$) peaks, where Ψ denotes the tilt angle of the texture goniometer. The peak (102) is used to confirm the epitaxial growth of the YBCO on the substrate while the (122)/(212) peaks are used

to study the twin state and strain in the films. The rocking curves were measured at the (005) position.

2.3 Characterization methods of magnetic properties

The magnetic moments of the YBCO films were measured using *Quantum Design Physical Properties Measurement System* with the *AC measurement system* -option with which the system works as a vibrating sample magnetometer. In short, the magnetic moment in the sample is induced with a superconducting magnet (up to 9 T) and then the magnetic moment is measured by vibrating the sample through a set of pick-up coils. This gives the DC magnetization of the sample. The AC magnetization of the samples can be measured by exciting the sample with an AC magnetic field and then measuring the response of the sample with the pick-up coils.

Typically, the DC magnetic moments of the YBCO films were measured from 8 T to -8 T and back at 10 K and 77 K. The AC magnetization of the YBCO films was measured from 100 K to 10 K in the AC field of 0.1 mT at 113 Hz frequency. The onset critical temperature, $T_{\mathrm{c}}^{\mathrm{onset}}$, is then defined as the temperature where the real part of the magnetization of the sample deviates from the background signal of the substrate which is the beginning of the transition from the normal state to the superconducting state in temperature.

Critical current densities of the YBCO films were calculated with Bean model [59]

$$j_{\mathrm{c}}^{\boldsymbol{B}||z} = \frac{2\Delta m}{L_x[1 - L_x/(3L_y)]V}, \tag{21}$$

where L_x and L_y are the dimensions of the rectangular sample ($L_x \leq L_y$), V is the sample volume and $\Delta m = m_-(\boldsymbol{B}) - m_+(\boldsymbol{B})$, where the subscript $+$ $(-)$ indicates that the DC magnetic moment has been measured in increasing (decreasing) field. The Bean model is based on a critical state model, which assumes that the current density inside a superconducting slab equals either j_{c} or zero. Furthermore, the Bean model assumes that j_{c} does not depend on magnetic field which leads the model to predict rectangular hysteresis loops. Flux pinning and magnetic history is included in the model within the assumption of the critical state, for example, if the sample originally has a zero magnetization and the field is then increased, the magnetization profile penetrates the sample starting from the boundary with the slope given by the critical current density. When the magnetic field is decreased back to zero, the magnetization in the sample decreases starting from the edges which leads to the situation where the magnetization reaches zero at the edges but not inside the sample. Thus, we get a positive total moment

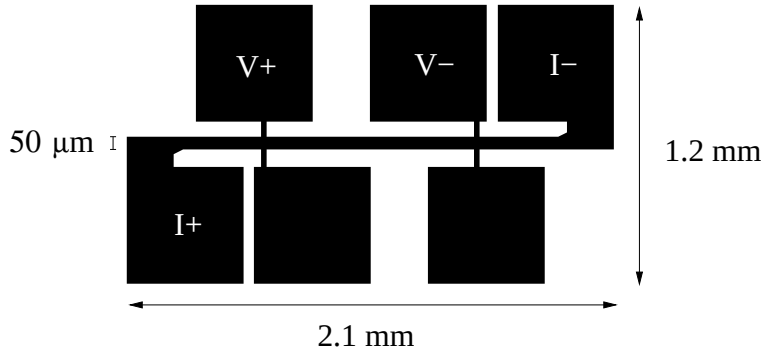

Figure 7. The pattern etched into the YBCO thin films for measurements in pulsed magnetic fields. The contact pads used in the four probe configuration have been labeled with $I\pm$ for current pad and with $V\pm$ for voltage measurement pad.

for the sample which depends only on the critical current density and geometry of the sample. Despite the rather oversimplified picture of the Bean model, it is useful for estimating the critical current density of the sample from magnetically measured data.

Since the upper critical field of YBCO is much higher than what can be reached with the magnetometer, a non-commercial pulsed magnetic field setup was used. The setup consists of a capacitor rack connected to a solenoid by a high voltage thyristor. The capacitance of the rack and the inductance of the solenoid have been chosen so that 2.1 kV charge in the capacitors will induce a 8 ms pulse of 30 T in the solenoid. The solenoid is immersed in liquid nitrogen to reduce the heating of the solenoid due to resistance and to keep the solenoid from melting.

To measure the resistance in high magnetic fields a circuit for four-probe measurement is etched on the YBCO thin film. The pattern etched on the film consists of a 50 μm current stripe and pads for making contacts. The pattern, as can be seen in figure 7, is very small because the sample is mounted on a sample holder with a rotating table so that the current is perpendicular to the magnetic field at all angles of the rotating table. Then the resistance of the film was measured with a 200 μA current during the magnetic pulse. The upper critical field and irreversibility field of the sample can then be determined from the data.

2.4 Solving the Ginzburg-Landau equations with flux pinning

Instead of directly solving the non-linear equations (5) and (6) we chose to minimize the energy functional (4) numerically. It is convenient to transform the integral (4) into a dimensionless form which can be achieved by the change of variables

$$\begin{cases} \widetilde{\psi} = \sqrt{\frac{\beta_{\mathrm{GL}}}{\alpha_{\mathrm{GL}}}}\psi \\ \widetilde{\boldsymbol{A}} = \frac{2e}{\hbar}\boldsymbol{A} \\ \widetilde{\boldsymbol{x}} = \frac{1}{\lambda}\boldsymbol{x}, \end{cases} \tag{22}$$

which gives a new functional

$$G_{\mathrm{s}}[\psi] = \int \mathrm{d}^3\boldsymbol{x} \left[\|(\nabla + i\boldsymbol{A})\psi\|^2 + \|\nabla \times \boldsymbol{A}\|^2 + \frac{1}{2}\kappa^2(|\psi|^2 - 1)^2 \right], \tag{23}$$

where the zero point of energy has been chosen so that the integrand is always non-negative. The $\boldsymbol{H} \cdot \boldsymbol{B}$ term has also been absorbed as a constant since $\boldsymbol{H}$ is assumed to be homogeneous and $\int \boldsymbol{B}\, \mathrm{d}^3\boldsymbol{x}$ is fixed by the boundary condition. Also, the constants before the integral have been left out since they do not affect the minimization of the functional. To discretize the fields a simple forward difference was used. But the forward difference was done utilizing exponential functions to preserve the gauge symmetry. The details of the gauge invariant discretization of the fields are described in [60]. In addition, the scaling of the functional to the form in (23) demonstrates nicely how the Ginzburg-Landau theory actually has only one free parameter, κ.

The equation (23) is then minimized by using a variant of the quasi-Newton method with BFGS (Broyden, Fletcher, Goldfarb and Shanno [61–64]) update formula for the Hessian approximation. These algorithms are provided by *Portable, Extensible Toolkit for Scientific Computation* (PETSc) and *Toolkit for Advanced Optimization* (TAO) which are massively parallel numerical libraries. The simulations were run on the supercomputer of *CSC — IT Center for Science Ltd* named *Louhi*. A typical simulation size was $500 \times 500 \times 50$ pixels with a lattice constant of 0.3ξ. Running on 64 processors it took about 10 hours for each magnetic field value for the simulation to converge. Even with such a small number of processors, simulating two types of defects at two different densities in 10 magnetic field values with 4 repeats of randomized positions takes over 10 years of (single) CPU time. Therefore, the need for parallel computation with a supercomputer is obvious. The magnetic field was fixed and ψ set to zero at all boundaries except in the x-direction where a periodic boundary condition was used. The magnetic field was parallel to z-direction.

The pinning sites were modelled by restricting the order parameter to a smaller value in the rod. Only z-axis aligned columnar pinning sites like nanorods and dislocations were used. For simplicity, the restriction of the order parameter was done by setting 0.1 as an upper limit for both the imaginary and real part of ψ. This leaves some freedom for $|\psi|$, for which the upper limit varies between 0.1 and 0.14 depending on the phase, but it is easier to implement than restricting the absolute value directly. The upper limit was not set to zero because the vortices are easier to see inside the pinning site if the upper limit is slightly larger than zero.

3 Structural properties of $YBa_2Cu_3O_{6+x}$ thin films grown on $NdGaO_3$ and MgO

3.1 Thickness dependent microcracks in YBCO films on $NdGaO_3$

The interaction between a twin boundary and a vortex is interesting because the twin boundaries are anisotropic planar pinning sites that can channel the vortex in the plane and hinder its movement perpendicular to the plane. In a typical undoped YBCO thin film grown on STO substrate, the twin boundaries grow biaxially making measurements along or normal to a twin boundary difficult. However, NGO substrate cut perpendicular to [001] direction gives a directional preference for the growth of YBCO which results in uniaxial twinning [65]. An example of biaxial and uniaxial twinning seen in XRD-measurements is shown in figure 8 where the biaxial twinning in YBCO on STO results in a four-peak system of (122)/(212) while in the uniaxial case of YBCO on NGO, the system shows only two peaks.

Unfortunately, the directional preference of the substrate causes the film to develop parallel microcracks that are normal to the twin boundaries [66]. Two sets of pulsed laser deposited undoped YBCO thin films were grown on NGO(001) to investigate the thickness dependence of the films. The other set was done using the nanocrystalline target (n-films) and the other using solid state target (µ-films). The AFM images in figure 9 show how the parallel cracks develop with increasing film thickness. The length of the parallel cracks that are visible in the AFM images varied from 50 µm to 1 mm being longer in thicker films. The separation between the cracks is about 2–5 µm in all the n-films. In the case of the µ-films, the cracks were hardly visible in the AFM, and their separation was larger.

The YBCO lattice is more strained in thinner films relaxing with film thickness. The full width at half maximum (FWHM) values of the (122)/(212) peaks in the φ-direction shown in figure 10 indicate a consistent relaxation of the YBCO lattice with increasing film thickness. Since the FWHM values in the 2θ had no similar trend it can be concluded that the relaxation involves the angles of the pseudo-orthorhombic YBCO rather than the values of the lattice parameters. The orthorhombic NGO (001) surface distorts the angles since the YBCO grows on it epitaxially but rotated by 45° [65].

The microcracks have a curious effect on the rocking curves measured from the YBCO (005) peak. The rocking curves shown in figure 11 were measured the incident beam normal to the cracks. The curves develop clear shoulders with increasing film thickness for the both series of films. The rocking curves are not only simply broadened

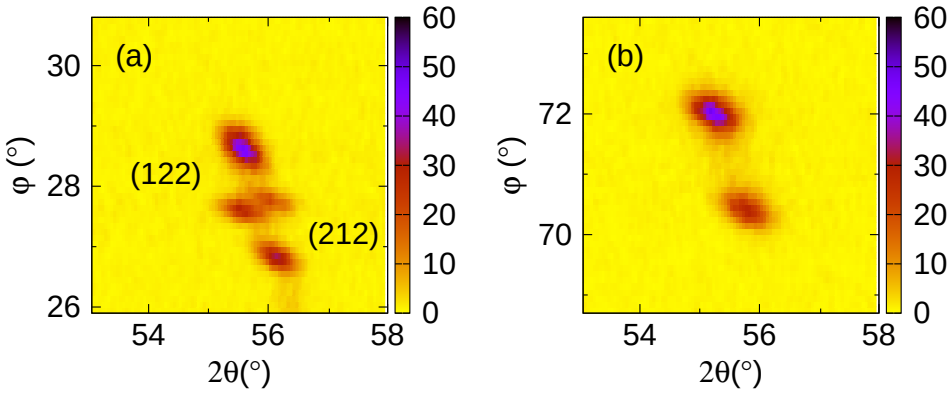

Figure 8. The twinned (122)/(212) XRD-peaks in a YBCO thin film grown on (a) STO(100) and on (b) NGO(001). The four-peak system in (a) is biaxially twinned while the case (b) is uniaxially twinned. [**P1**]

by the microcracks but also show three distinct peaks. The shoulders indicate that the YBCO lattice has two favoured alignments slightly skewed from the usual epitaxial one. This skewing is most prominent in the thickest films and could be connected to the additional shapes seen around the cracks in the AFM images in figure 9.

To calculate the critical current densities of the samples the magnetic moments of the samples were measured. Since NGO is strongly paramagnetic at low temperatures, the diamagnetic signal of the sample needs to be resolved from the signal of the substrate. This is achieved by taking half of the opening of the hysteresis loops as the moment of the sample. The magnetic moments of the samples at 40 K in self-field are shown in figure 12. The moments should increase with increasing film thickness since the volume of the sample increases but, in this case, the cracking of the films cuts the paths of the supercurrents and the total moment decreases instead. The µ-films show a drastic drop between the two thinnest films which could be a threshold at which the cracking occurs. Nonetheless, the j_c of the thinnest µ-film is still four times smaller than the value of the 190 nm thick reference film on STO. The difference is partly due to the thinness of the film since j_c deteriorates quickly for films below 100 nm thickness [67, 68]. With n-films, if such a cracking threshold exists, it would be at thinner thicknesses than 70 nm.

The critical current density of the films is usually calculated from the magnetic data using the Bean model (equation 21). In this case, the Bean model cannot be applied directly since the samples are not intact. Assuming that the sample is divided into many parallel slabs that have the width (w) of the crack separation seen in the AFM images

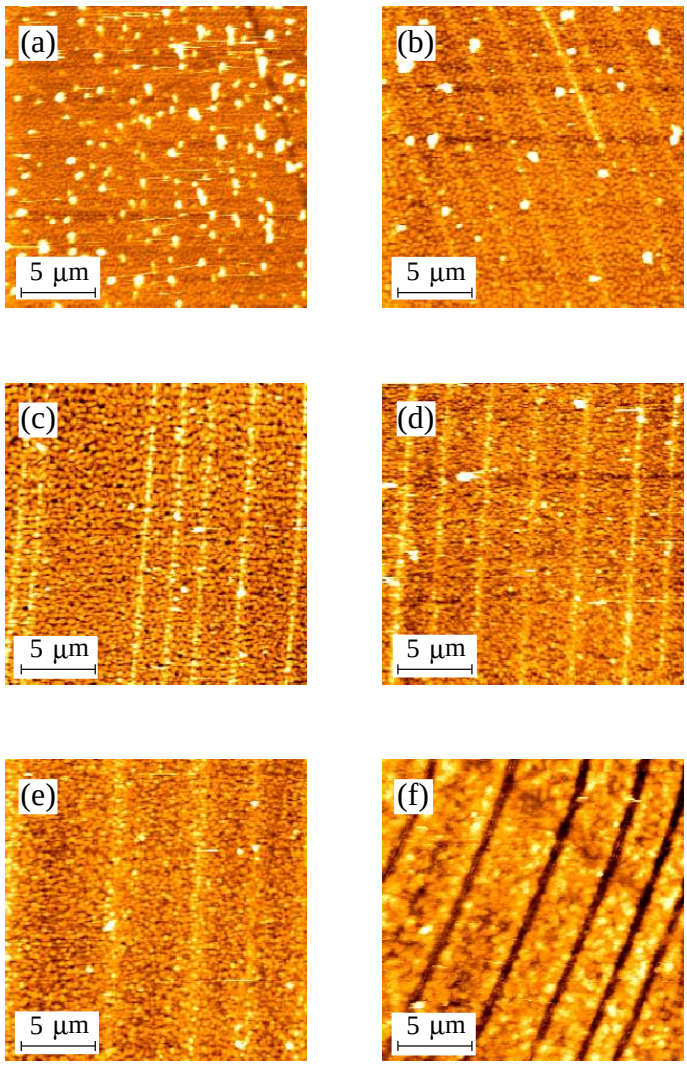

Figure 9. Parallel cracks seen in n-films on NGO of thickness (a) 70 nm (b) 100 nm (c) 130 nm (d) 180 nm (e) 330 nm. The last image (f) is from the same film as in (e) but the film surface has been partially etched away by phosphoric acid. The height scale from black (low) to white (high) in the images is 50 nm in a, b, f and 20 nm in c, d and e. [**P1**]

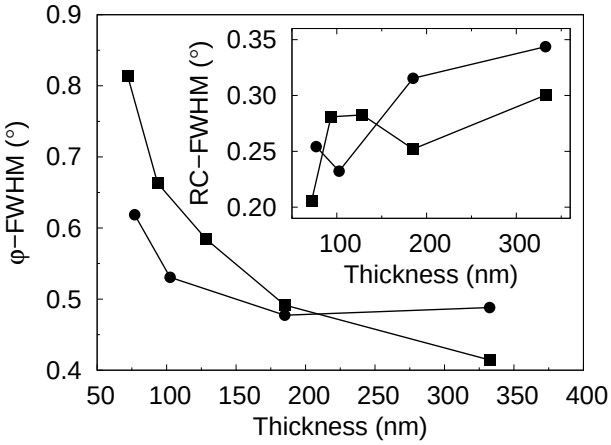

Figure 10. The FWHM values of the (122)/(212) peaks of the YBCO films on NGO as a function of film thickness. The n-films are indicated with circles (●) and the μ-films with squares (■). Inset: FWHM values of the YBCO (005) rocking curves shown in figure 11. [**P1**]

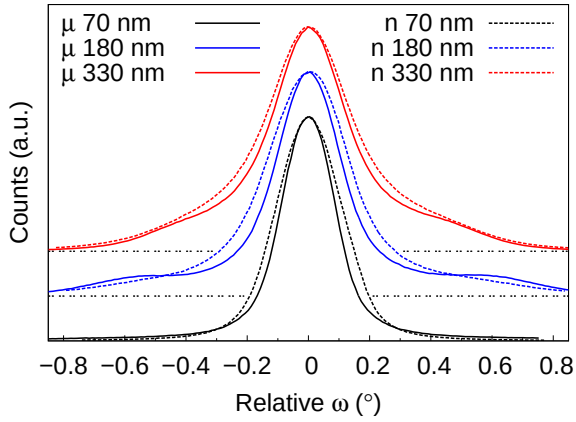

Figure 11. The YBCO (005) rocking curves measured incident beam normal to the microcracks. The solid lines are for the μ-films and the dashed lines for n-films. The horizontal dashed lines mark the base levels of the curves that have been offset for clarity. [**P1**]

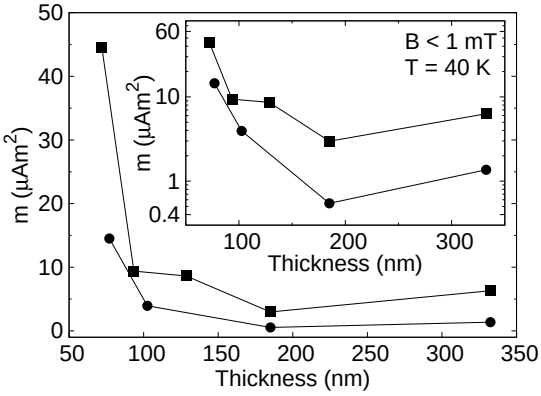

Figure 12. The magnetic moments of the samples at 40 K in self-field. The inset shows the same data with half-logarithmic scale. The n-films are indicated with circles (●) and the μ-films with squares (■). [**P1**]

and that have the length of the whole sample (L_y), we can estimate the local critical current density using the Bean model. If the cracks divide the sample into N pieces and if the magnetic signal from one piece is $\Delta m'$ then the measured signal from the sample is $\Delta m = N\Delta m'$. The Bean model gives the local critical current density for one piece as

$$j_{\mathrm{c,local}} \approx \frac{2\Delta m'}{w^2 L_y d} = \frac{2\Delta m}{N w^2 L_y d}, \tag{24}$$

where d is the thickness of the sample and where it has been approximated that

$$1 - \frac{w}{3L_y} \approx 1. \tag{25}$$

Using $N = L_y/w$ in equation (24) we get

$$j_{\mathrm{c,local}} \approx N\frac{2\Delta m}{L_y^3 d} = \frac{2\Delta m}{N^2 w^3 d}. \tag{26}$$

This estimate gives about 10 MA/cm^2 for the two thickest n-films with the average crack separation of 5 μm. With the μ-films a similar estimate is difficult since the cracks are not easily seen in the AFM images.

The n-films have a more rigid lattice than the μ-films which can be seen from the higher density of dislocations [69]. The difference in the elasticity of the films is the reason why the n-films have more pronounced cracks and a different cracking threshold than the μ-films. With μ-films the magnetic moment of the thinnest film indicates that the currents are able to circulate through the whole film without cracks cutting the current path. Thus, the thinnest μ-film either has no cracks at all or only very few and small cracks.

3.2 Microcracks in YBCO films on MgO

The lattice mismatch of YBCO with the cubic substrate MgO is quite large, about 9%, which can lead to microcrack formation in the YBCO films [70]. However, the low loss tangent of MgO makes it a good candidate for microwave applications, like resonators and filters, if the problems related to the lattice mismatch can be overcome. A series of 150 nm thick YBCO thin films were made on MgO to investigate the dependence of the microcrack formation on the deposition temperature and frequency. The deposition temperature was varied between 650 °C and 850 °C with steps of 50 °C and the deposition frequencies were 1, 2, 5, 10 and 20 Hz. All the films were made from the same nanocrystalline undoped YBCO target and were grown to 150 nm thickness.

Below the deposition temperature of 800 °C, there are no microcracks visible in the AFM images. In the case of 800 °C, the microcracks are visible only at 10 and 20 Hz. As is shown in figure 13, the cracks in the films deposited at 800 °C are short in length, typically between 1 and 5 µm, and do not penetrate through the whole film thickness. The widths of the cracks are relatively large, almost half a micrometre. The height profile in the figure 13 also shows that additional material accumulates near the edges of the microcrack. It is possible that the additional material is due to a partial melting of YBCO. It has been shown that by decreasing the partial pressure of oxygen the melting point of YBCO can be as low as 800 °C and at the deposition pressure the melting temperature would be about 870 °C [71].

There are microcracks visible at all frequencies in the films deposited at 850 °C. These cracks are oriented at an angle of $\pm 45^\circ$ to the substrate a-axis. The cracks are longer than in the 800 °C case, being about 15–30 µm in length. Unlike in the 800 °C films, the cracks also penetrate through the whole film thickness down to the substrate at low frequencies. With increasing frequency these cracks fill up until at 20 Hz they look like ridges instead of cracks. The filling of the microcracks with increasing deposition frequency can be seen in the series of AFM images in figure 14.

When growing on the MgO substrate YBCO tends to form grains rotated by 45° in-plane. This rotated phase suppresses the superconductivity in YBCO quite a lot [72]. The XRD measurements on the samples showed that the samples deposited below 750 °C contained virtually no 45° oriented phase at all. At 800 °C the rotated phase already dominates in the growth. Otherwise, the appearance of the 45° oriented phase goes hand in hand with the appearance of the microcracks except when increasing the frequency the cracking increases but the amount of the rotated phase decreases. The cracking and the rotation are connected because they are both stress relieving mecha-

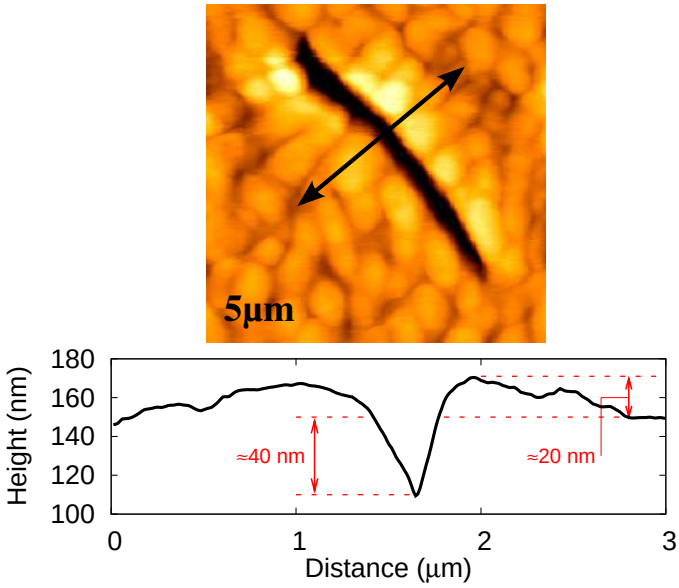

Figure 13. AFM image of the microcrack in YBCO thin film deposited at 800 °C with pulse frequency of 10 Hz. The image size is 5×5 µm^2. [**P2**]

nisms that may compete with each other when the growth dynamics is changed by the parameters.

Naturally, the extensive cracking of the YBCO thin films is seen as a dramatic worsening in the superconducting properties of the samples. The critical current densities of the samples calculated with the Bean model, assuming that it would be applicable in spite of the cracks, are shown in figure 15. The optimal deposition temperature to maximize the critical current density is at 700 °C or slightly above. At 700 °C the optimal range extends from low frequency up to 5–10 Hz unlike at other temperatures where the critical current density drops quickly with increasing frequency. Below 700 °C the critical current density drops gradually because of the too low deposition temperature while above 750 °C the drop is drastic because of the cracking of the films.

In contrast, the critical temperatures of the samples are not so sensitive to the cracking. The optimal deposition temperature would be at 750 °C for maximal critical temperature with a gradual decrease in both directions in the deposition temperature. The best onset critical temperature is slightly above 88 K while the worst goes down to 72 K. The optimal range also extends to larger frequencies than in the critical current case. On the other hand, the cracking induces a multitude of weak links in the samples which is seen as a strong increase in the superconducting transition widths of the samples above

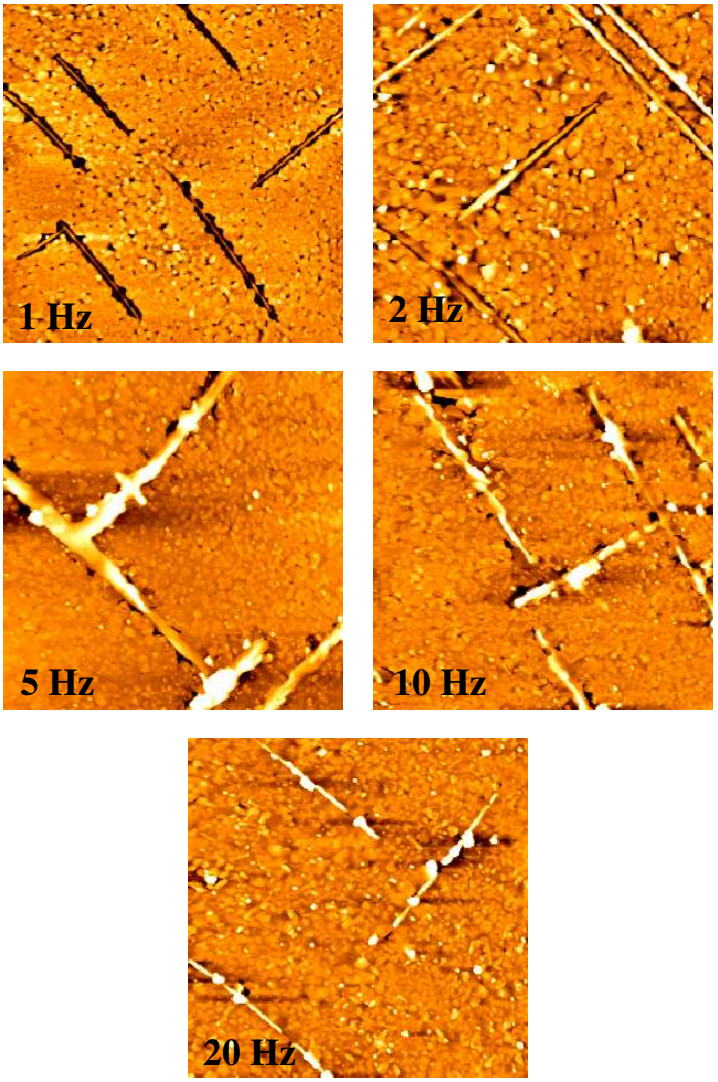

Figure 14. AFM images of the films deposited at 850 °C with different pulse frequencies from 1 Hz to 20 Hz. The sizes of the images are 50 × 50 μm^2. The cracks visible in the figures are rotated by 45° compared to the a-axis of the substrate. [**P2**]

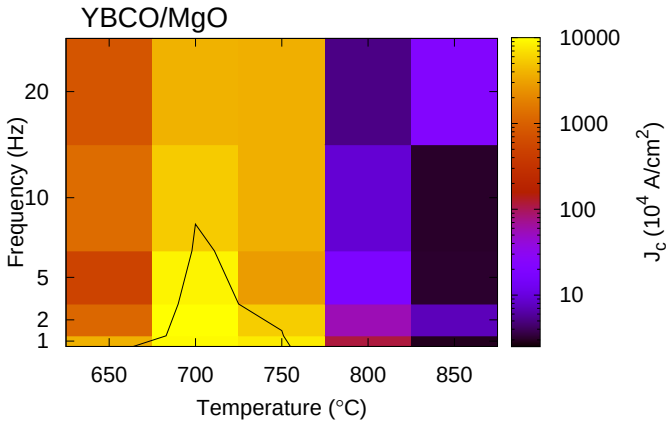

Figure 15. The critical current densities of the YBCO thin films deposited on MgO as a function of the deposition temperature and frequency. The solid line is an approximated contour of 50 MA/cm^2. [**P2**]

750 °C. The transition widths are below 3 K for the films in the optimal areas while the widths are broadened to 20–40 K with the cracking of the films at 800 °C and above. Increasing the deposition frequency increases the transition width slightly in all cases.

In short, the higher thermal energy at the deposition temperatures above 750 °C induces the rotation of the YBCO lattice by 45° and simultaneously the microcracks are formed. These relaxation mechanisms are induced by the relatively large lattice mismatch of the YBCO thin film with the MgO substrate. As it was shown, it is possible to optimize the growth conditions so that the rotation of the YBCO lattice and the formation of the microcracks are suppressed.

3.3 Comparison of the microcracks

The formation of microcracks is a general concern with thin film methods which needs to be addressed with a careful choice of the substrate and possible buffer layers. In the case of PLD thin films the main reasons for the cracking to occur are either too large lattice mismatch or too different thermal expansion coefficients with the film and the substrate. Of the discussed cases of microcrack formation in YBCO films on NGO and MgO, the MgO case falls into the first category and the NGO case into the second. However, the situation is more complicated since the cracks do not appear in all of the films. In this work, the microcrack formation was seen to be triggered by the film

thickness in the NGO case and by the deposition parameters in the MgO case.

The microcracks are much wider in the films on MgO than on NGO while the length of the cracks is similar in both cases. Additional material grows inside the cracks in the MgO case, so it can be said that the films crack already during the deposition. In the NGO case, the cracking probably occurs during the cooling because the thermal expansion coefficients in the b-direction between YBCO and NGO ($8.7 \cdot 10^{-6}$/K [73] and $2.3 \cdot 10^{-6}$/K [74], respectively) are quite different, while they are similar in the a-direction ($11.0 \cdot 10^{-6}$/K [73] and $11.3 \cdot 10^{-6}$/K [74], respectively). Also, the uniaxial twin structure is formed during the cooling which complicates the situation. The direction of the microcracks is connected to the direction of the twins in the NGO case and to the formation of the 45° phase in the case of MgO.

4 Anisotropy and flux pinning in $BaZrO_3$ doped YBCO thin films

4.1 The magnetic field dependence of the critical current density

The big challenge for material scientists in general is the ability to give predictions of the properties of possible new materials. With superconductors one such challenge is understanding the reasons and mechanisms behind the critical current density of the material. Especially the angle and field dependence of the critical current density is of interest. The conventional approach to solve the critical current density given by a certain pinning site is a statistical one. Either statistical in the thermodynamical sense as in the work of Blatter *et al.* [11] where the vortices are often treated as particles or statistical in the sense that the path of the vortex inside the superconductor is thought of as a statistical distribution of jumps from one pinning site to the next. The latter is called a vortex path model [14, 75–78].

The vortex path models introduce the concept of the so-called trapping area which is the area around the pinning site where the attractive force of the pinning site is large enough to overcome the elasticity of the vortex lattice and thus the vortex is trapped into the pinning site. The statistical parameters of the distributions of the vortex paths are then fitted to the measured data to analyze, for example, the angle dependence of the critical current density further. The point is to try to separate the effects of the different types of pinning sites present in the sample. While the vortex path model is successful in many aspects of separating the effects from the different pinning sites, it still cannot give detailed information about the path of a single vortex through a certain pinning site. It gives only statistical averages. When the flux pinning is modelled with Ginzburg-Landau simulations the path of the vortex is seen in detail and also it is possible to test the effect of different parameters of the pinning landscape on the critical current density. On the other hand, with the simulations it is challenging to show that the model actually corresponds to the real system that you have measured since the model cannot include the whole real sample with its every detail.

For our YBCO samples made with PLD, the relevant pinning sites are the columnar ones when the magnetic field is parallel to the c-axis. Thus, the magnetic field dependence of the critical current density of the YBCO thin films at that angle was modelled as having only columnar pinning sites. The nanorods represent dislocations in an undoped sample or BZO nanorods in the doped case. Figure 16 shows an example of a simulation result with dislocations as the modelled pinning sites. The positions of the

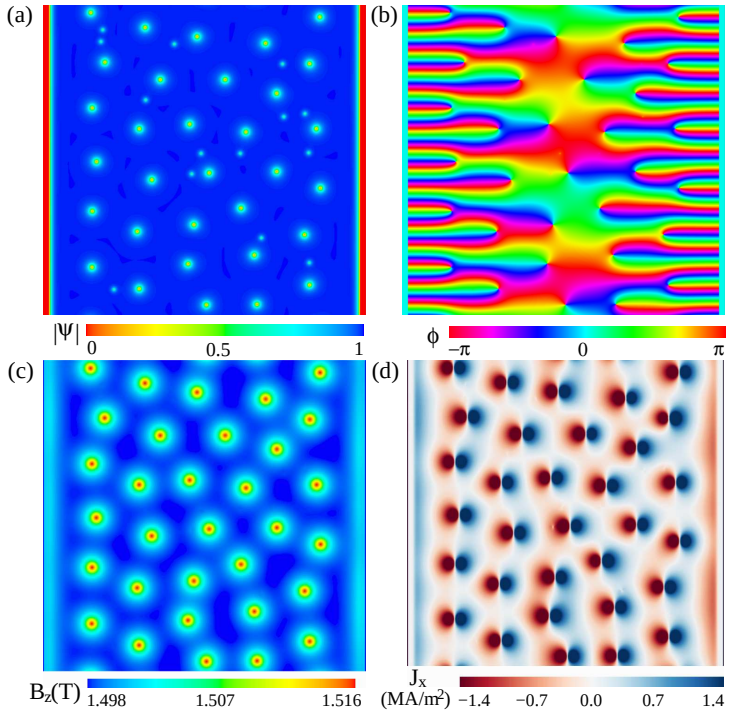

Figure 16. An example of the simulation result shown as a cross-section perpendicular to the c-axis. The magnetic field (1.5 T) is parallel to c-axis. (a) The absolute value and (b) the phase of the order parameter. (c) The component of the magnetic flux density perpendicular to the slice. (d) The component of the current density that is parallel to the periodic direction. The boundaries at left and right are in vacuum while the top and bottom are periodic boundaries. The scale of the current density is saturated so that the shielding current at the edges is also visible. [**P3**]

dislocations were randomly chosen from a uniform distribution. The empty pinning sites can be seen as the small dots in figure 16(a) which shows the absolute value of the order parameter. The phase of the order parameter, the magnetic flux density and current density calculated from the vector potential are also shown in figure 16. In addition to the currents circulating each vortex, there is also a shielding current visible in the image at the edges of the simulated sample.

The case of BZO doped YBCO was modelled with nanorods that had a diameter of 5 nm while the diameter of a dislocation was modelled as 0.3 nm [47, 79, 80]. The densities of the dislocations used in the simulations were 90 mT, 180 mT and 360 mT which are reasonable values for YBCO PLD films [81]. The critical current density was simulated at different magnetic field values starting from the high field and using the

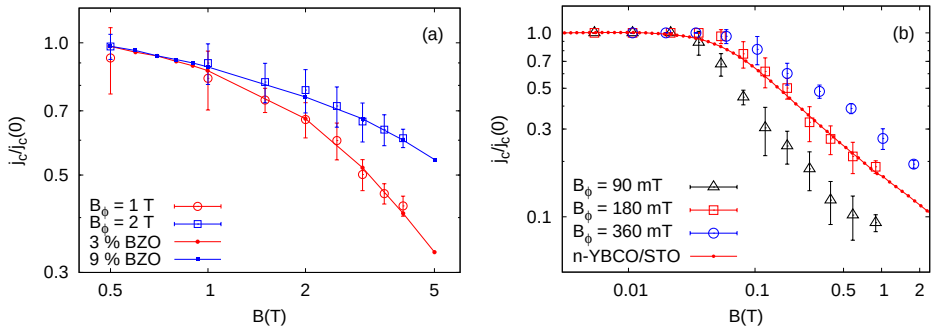

Figure 17. (a) The simulated j_c caused by the BZO nanorods at the number densities of 1 and 2 T which are compared to experimental j_c of 3% and 9% BZO doped YBCO thin films. (b) The simulated j_c caused by the dislocations at the number densities of 90, 180 and 360 mT compared to an undoped YBCO thin film. The experimental data is shown as linespoints and the simulation results are the point with errorbars. [**P3**]

end result of the simulation as the starting point for the next one at a lower field value. This procedure was repeated four times with different randomized positions for the nanorods. From the simulation result it was then checked which vortices are pinned and how many are free. The ratio of the pinned vortices to total number of vortices was taken as the normalized critical current density [75]. The averages of the simulation results are shown in figure 17 where the errorbars show the standard deviation of the results between the repeated simulations. The experimental data fits well within the errorbars of the data points from the simulations. The j_c-data of the BZO nanorods show a general rounded shape while with dislocations there is a clear kink at the accommodation field. This difference is partly explained by the higher density of the BZO nanorods than the dislocations which makes the role of vortex-vortex interactions more important.

The higher density is not the only difference between the BZO nanorods and dislocations. Namely, the dislocations are considerably smaller in size, too. The effect of the rod size was investigated with a series of simulations with different rod size but the same density of nanorods. The density was chosen as a compromise between the densities used in the BZO simulations. The simulated critical current densities for the different rod sizes are shown in figure 18(a). The shape of the j_c-curve has a more rounded shape at large rod sizes than at small. It can then be concluded that the typical rounded shape of the critical current density of a BZO doped sample is caused by the large rod size in addition to the high density. The j_c-curves were further analyzed by fitting the power-law with the exponent α to the part of the curve that is close but

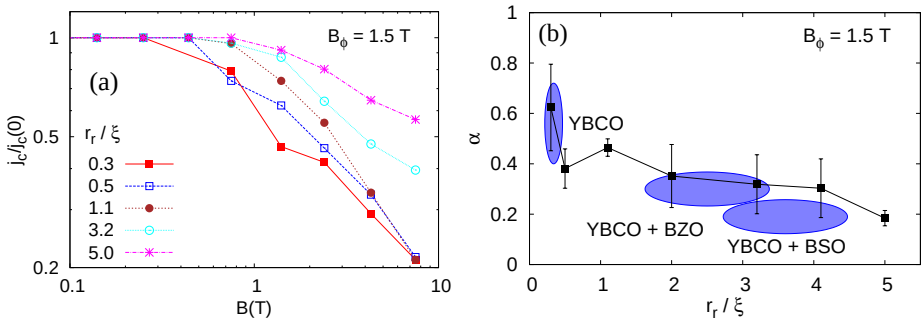

Figure 18. (a) The simulated magnetic field dependence of the critical current density with different nanorod radii r_r. (b) The α-values obtained by fitting the power-law to the critical current density data. The experimental values shown as the ellipses were measured from undoped [82, 83], BZO-doped [69, 84, 85] and $BaSnO_3$-doped [43, 44] YBCO thin films. [**P3**]

still above the accommodation field. The fit results are shown in figure 18(b) where the experimental values for various types of YBCO films are also shown as ellipses for comparison. The agreement between the simulation results and the experimental values is fairly good although the simulation seems to underestimate the pinning strength a bit leading to too high α-values. This is natural since the real samples have other types of pinning too in addition to the simulated nanorods.

The pinning problem is further complicated by the possibility that more than one vortex can be pinned to the same pinning site. Multiple occupancy of the pinning sites is naturally more probable with larger pinning sites. Indeed, with the increasing size of the nanorods up to four vortices were seen to occupy the same nanorod. Examples of the vortex lattice with different nanorod sizes are shown in figure 19. When there are several vortices in the same pinning site, they do not form a giant vortex with a single shared core but sit symmetrically on the opposite sides of the rod near the edges. At rod size $r_r = 2\xi$, the small size of the vortex forces the two vortices very close to each other making it very difficult to say whether the vortices are separate or not. At smaller nanorod sizes there is only one vortex per rod.

The large nanorods are strong pinning sites which also disturb the triangular vortex lattice. With increasing rod size the vortex lattice loses its long range order, which can be seen in the radial distribution functions shown in figure 20. At small rod size, four broad peaks can be seen in the distribution corresponding to having a long range order up to the seventh nearest neighbour in a triangular lattice. Increasing the size of the

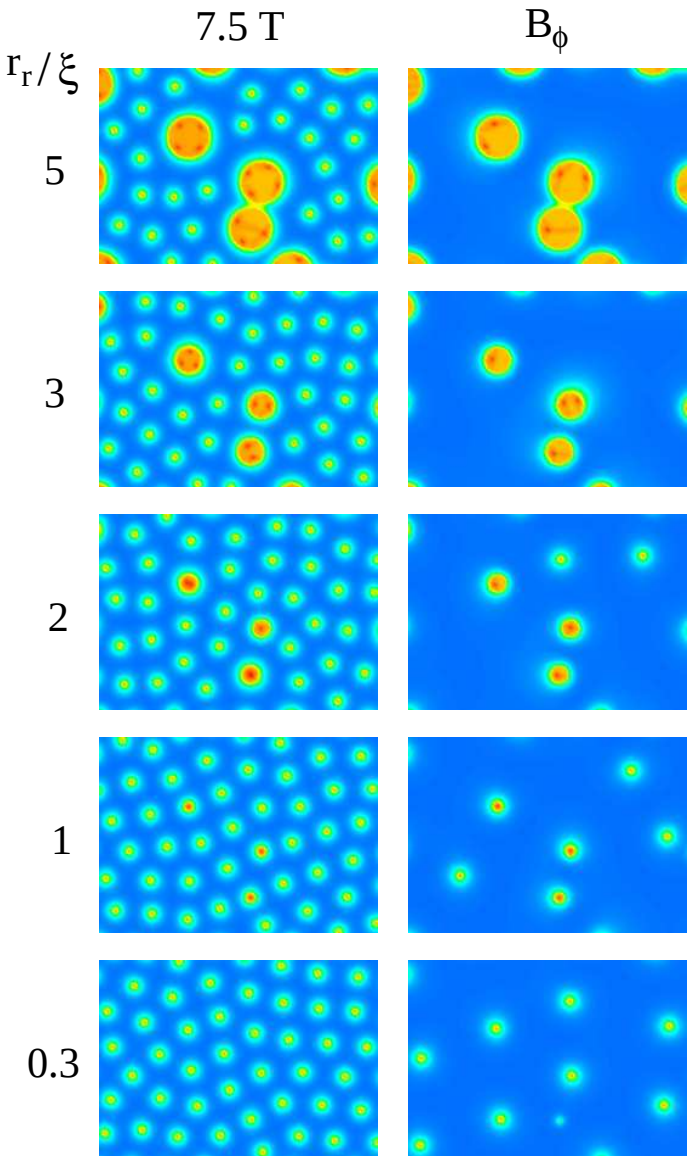

Figure 19. A visualization of the effect of increasing nanorod size on the vortex lattice at 7.5 T (left) and at matching field (right). The colour describes the absolute value of the order parameter with same scale from 0 (red) to 1 (blue) as in figure 16. The radii of the nanorods (r_r) increase in size from bottom to top as indicated by the number on the left. [**P3**]

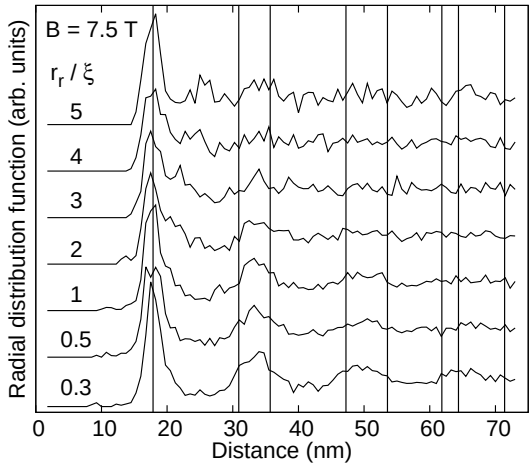

Figure 20. The radial distribution functions calculated from the vortex positions at 7.5 T with different nanorod sizes. The vertical lines are set at the theoretical nearest neighbour positions of a triangular vortex lattice. [**P3**]

nanorods destroys the long range order leaving only the nearest neighbour peak of the short range order visible at large rod size. Similar disturbance in the vortex lattice near a pinning site and the pinning of more than one vortex in the same pinning site can also be seen in the experiments [86].

The Ginzburg-Landau equations combined with the model for the pinning sites can be used as a tool to distinguish the importance of the various sources of pinning in the material. The question of optimal pinning landscape is far from trivial, in addition to the vortex-vortex interactions, the situation is further complicated by the interplay of strong pinning in the nanorods and collective pinning in weaker pinning sites. In the case of magnetic field parallel to the nanorods, the dominating role of the flux pinned in the columnar pinning sites can be used to simplify the situation. Here it has been shown that it is enough to model only the columnar pinning sites to reproduce the experimental magnetic field dependence of the critical current density in YBCO thin films. If the magnetic field is not parallel to the columnar pinning sites the model needs to be improved by i) adding other relevant types of pinning sites, for example, twin boundaries ii) replacing the simplified method of calculating the critical current density with a real transport current. The improvements are needed to account for the interplay of an inclined vortex with many types of competing pinning sites.

4.2 The effect of $BaZrO_3$ doping on the anisotropy of YBCO

One of the biggest drawbacks of high temperature superconductors is the high anisotropy caused by their layered structure. The aim of pinscape engineering is to modify the pinning landscape to compensate the high anisotropy with anisotropic pinning sites, for example, columnar nanorods [38, 45]. In the case of YBCO thin films grown with PLD, the anisotropy is often balanced by BZO doping which improves the critical current density, especially when the magnetic field is parallel to the c-axis [42]. The improvement of the j_c also means that the fitting of the effective anisotropy, γ_{eff}, gives low values with BZO doped samples. Therefore, the question arises whether the anisotropy of intrinsic quantities, for example the upper critical field, is lowered by the doping too.

In this work, the upper critical field and the irreversibility field were measured with a four-point resistance measurement in pulsed magnetic field. The measured samples were two undoped YBCO PLD films, one grown with n-target (grainsize in nanometre scale) and the other with µ-target (grainsize in micrometre scale), and a 5 wt-% BZO doped YBCO film. The angle dependence of the magnetoresistance of the samples was measured at $T = 0.96\ T_c$ and at $T = 0.90\ T_c$. The measurement temperatures were fixed with the reduced temperature scale to compensate for the different critical temperatures of the doped (85 K) and undoped samples (89 K). An example of the measured resistivity curves is shown in figure 21.

The resistivity data was analyzed by fitting the curve shape with the function [87],

$$\rho(B,T,\theta) = [\rho_0(T) + a(T,\theta)B] \exp\left[-\frac{U(T,\theta)}{B^{n(T,\theta)}}\right], \tag{27}$$

where $\rho_0(T)$ is the normal state resistivity, $a(T,\theta)$ is the coefficient for the linear normal state magnetoresistance and $U(T,\theta)$ and $n(T,\theta)$ are fitting parameters accounting for the shape of the superconducting transition. The normal state resistance, $\rho_0(T)$, is assumed to be independent of the angle while all the other parameters depend on it. After fitting equation (27) to the data, it is then easy to calculate the upper critical field from the fitting parameters. In calculating the upper critical field only the exponential part of equation (27) was used because it is the part that describes the transition to the superconducting state. Using only the exponential part, the upper critical field can then be calculated as

$$B_{c2} = B_0 + \frac{1 - f(B_0)}{f'(B_0)}, \tag{28}$$

where

$$f(B) = \exp\left(-\frac{U}{B^n}\right), \tag{29}$$

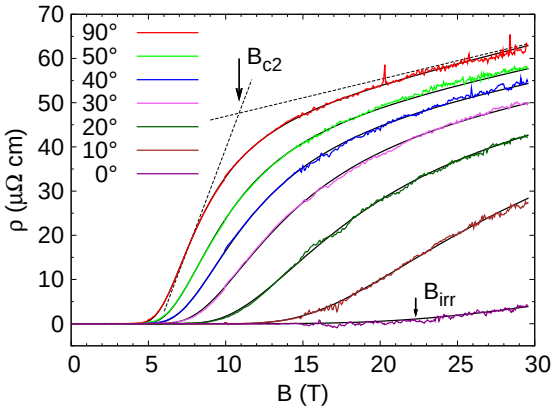

Figure 21. The magnetoresistance of the μ-film at 80 K at different angles. The topmost curve is at the field out of plane position (90°) while the curve at the bottom is the field in plane configuration (0°). The equation (27) fitted to the data is shown as solid black curves. The dashed lines show an example how the upper critical field is determined from the fit. [**P4**]

and $f'(B)$ is its derivative

$$f'(B) = \frac{nU}{B^{n+1}} \exp\left(-\frac{U}{B^n}\right), \tag{30}$$

and B_0 is the root of the second derivative $f''(B)$ resulting in

$$B_0 = \left(\frac{nU}{n+1}\right)^{\frac{1}{n}}. \tag{31}$$

The equation (28) for the upper critical field can be derived by calculating the crossing point of the tangent drawn through the zero point of the second derivative at B_0 and the asymptote line of the exponential part of the fitting function. Since the normal state resistance has been normalized and only the exponential part is used, the asymptote is one. This definition of the upper critical field is similar to the one used in [88] and is also demonstrated by the dashed lines in figure 21.

The calculated upper critical field values agree well with the Blatter scaling (equation 18) as is shown in figure 22a. In addition, the data for the undoped films are quite close to each other while the BZO doped film has higher upper critical field at all angles. A similar unexpected enhancement of the upper critical field has also been observed in $GdBa_2Cu_3O_{6+x}$ films doped with $BaHfO_3$ [89]. The dopant grows as columnar nanorods in the material in both cases which could be linked to the increased upper critical field. However, some caution is needed when interpreting the results because the

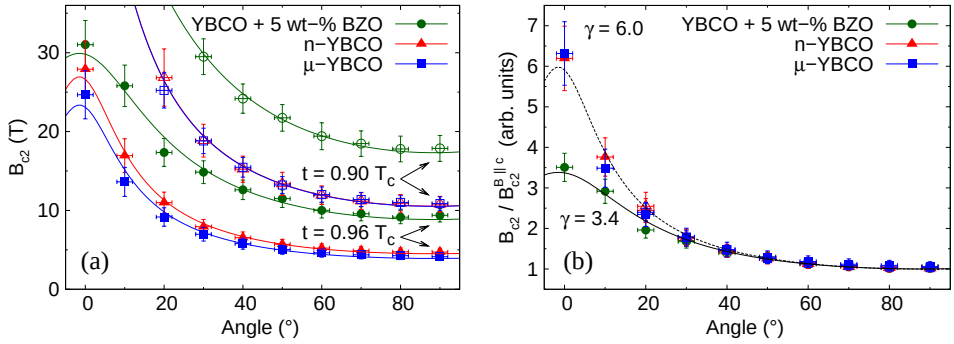

Figure 22. (a) The upper critical fields of the YBCO thin films obtained from fitting the resistivity data as a function of the angle between YBCO ab-axis and the magnetic field. The solid lines are fits of equation (18) to the data. The temperatures given are relative to the onset critical temperature. (b) The normalized upper critical fields of the YBCO thin films. The dashed line is a common fit to the both undoped YBCO films while the solid line is a fit to the BZO doped film. [**P4**]

data has been measured at different temperatures that are the same only in the reduced temperature scale. The problem is that the transition width of the BZO doped sample is larger than in the undoped films. Thus, choosing the definition of the critical temperature affects the results. It is not clear whether the onset critical temperature that was used here was the right choice. On the other hand, the temperature derivate of the upper critical field is increased by 40% by the BZO doping which supports the claim that the enhancement of the upper critical field is real.

The differences in the angle dependences of the upper critical field between the samples can be better seen when the data is normalized by the field out of plane values as is shown in figure 22b. The data for the undoped samples follow closely the same curve so the Blatter scaling was fitted to both of the films with the same anisotropy coefficient $\gamma = 6.0 \pm 0.2$. For the BZO doped sample the fit gives a 40% lower value resulting in $\gamma = 3.4 \pm 0.2$. According to equation (11), the anisotropy of the upper critical field translates directly to the anisotropy of the coherence length which in turn can be written as [8]

$$\xi^2 = \frac{\hbar^2 n^*}{4m\mu_0 H_c^2}, \tag{32}$$

where H_c is the thermodynamical critical field and n^* is the density of the Cooper pairs that has been assumed to be uniform. In equation (32) the effective electron mass is the only quantity that can have anisotropy hence the anisotropy coefficient γ measures

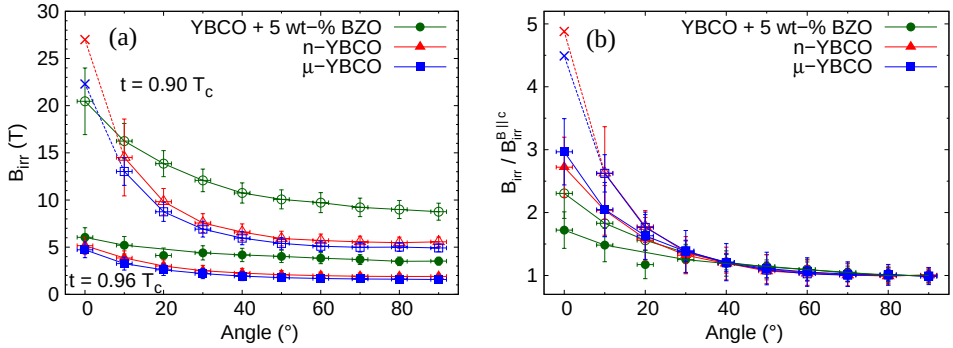

Figure 23. (a) The irreversibility fields of the YBCO thin films obtained from fitting the resistivity data as a function of the angle between YBCO ab-axis and the magnetic field. The data with open symbols were measured at 0.90 T_c and the closed ones at 0.96 T_c. The crosses at 0° are points where a good fit was not possible and the values were estimated with 1 mV/cm criterion directly without fitting. (b) The normalized irreversibility fields of the YBCO thin films. The two temperatures are marked with open and closed symbols as before. [**P4**]

directly the anisotropy of the electrons. The mechanism behind the change in the electron band structure is quite likely the same as with the enhancement of the upper critical field. Somehow the BZO nanorods affect the electron band structure of YBCO which is unexpected because the BZO does not react with YBCO but forms a separate phase. Two separate groups, Llordés *et al.* [88] and Miura *et al.* [90], observed no change in the effective electron mass in BZO doped YBCO films but the measured films were not made with PLD and the BZO grows differently into 3D particles with their methods. Perhaps the shape of the BZO nanorods plays also a role in the change of the anisotropy with doping.

The irreversibility field B_{irr} was defined as the field value where the resistivity in the transition is at 1% of the normal state value which is easy to calculate from the fitted parameters of equation (27) to be

$$B_{\mathrm{irr}} = \left(\frac{U}{\ln 100} \right)^{\frac{1}{n}}. \tag{33}$$

The 1% criterion corresponds roughly to a 1 mV/cm when expressed in voltage. This is larger than the typical 1 μV/cm criterion used because the samples are very small. With a short sample the same voltage criterion is stricter than with a long wire sample, because the long wire gives a stronger signal while the noise level is roughly the same

for both cases. The irreversibility field values calculated from the fits are shown in figure 23a. The BZO doped sample has the highest values at almost all angles while the undoped films have lower values. The high B_{irr} values are due to the enhancement of flux pinning with BZO doping which is most efficient in the field out of plane case.

The irreversibility field data does not agree with the Blatter scaling law. The values are too large near the field in plane position when compared to the fitting function. In addition, the data does not even fall on the same angular dependence when normalized as can be seen in figure 23b. Trying to analyze the data with an anisotropy parameter would lead to a temperature dependent γ. The normalized data also shows how the BZO doping lowers the anisotropy of the pinning landscape in the film which is a desired effect for the material in applications. The fact that the irreversibility line does not agree with the Blatter scaling has also been shown before for undoped YBCO by others [91].

4.3 Side effects of the $BaZrO_3$ addition

In improving the flux pinning in YBCO, introducing artificial pinning sites by doping with BZO has proved quite successful. In addition, the BZO nanorods cause a multitude of effects on the properties of YBCO. Through the enhancement of flux pinning the anisotropy and the field dependence of the critical current are reduced. The Ginzburg-Landau equations can be used to analyze these effects caused by flux pinning and complex interactions in vortex dynamics. The simulations give the insight that it is the size of the columnar pinning site that is an important factor in the characteristics of the field dependence of the critical current density and also in the change of the ordering of the vortex lattice. However, the changes seen in the effective mass of electrons and the enhancement of the upper critical field are unexpected side effects of the BZO doping. Since the upper critical field is an intrinsic quantity, the Blatter scaling is valid and describes the angular dependence well. In contrast, the extrinsic irreversibility field cannot be fitted with the Blatter scaling. Thus, the angular dependence of the critical current density should not be fitted with Blatter scaling, either. In practise, the Blatter scaling can still be used in a sort of background subtraction that accounts for the isotropic pinning present in the sample. The validity of such a background subtraction is difficult to verify and also there is the question of the anisotropy parameter. Should the value of undoped or doped YBCO be used in the subtraction?

5 Ginzburg-Landau simulations on giant vortex states in thin type I films

In addition to the challenges related to the flux pinning, there is also great complexity in vortex structures formed in confined superconductors and in type I materials. These typically include vortices carrying more than one flux quantum. A vortex with multiple flux quanta is called a giant vortex if it is cylindrically symmetric and a multivortex otherwise. These exotic multiquanta vortex structures have been observed in confined superconducting systems and in thin Pb films with and without artificial pinning sites [92–97]. In general, a giant vortex is energetically unfavourable since the magnetic energy of many non-interacting singly quantized vortices is proportional to NB^2, where N is the number of flux quanta (number of vortices) while the magnetic energy of one giant vortex is proportional to $(NB)^2$ [6]. But these naive arguments overlook the energy of the superconductor-normal interface which explains why giant vortices are often seen in the experiments under special circumstances, for example, in thin lead films.

In the 1960's it was observed that the critical field of a type I superconducting thin film is higher than the bulk value. Tinkham proposed that the presence of vortices is behind the effect [98]. Maki and Lasher did the theoretical work based on linearized Ginzburg-Landau equations showing that the Abrikosov lattice is a solution for all values of κ if the thickness of the sample is taken into account and that the solution can have giant vortices [98, 99]. With the current numerical methods the problem of giant vortices in type I superconductors can be addressed with the full nonlinear Ginzburg-Landau equations.

A thickness series of thin films was simulated for two values of κ (0.5 and 1.0). Two pinning sites were also included to break the translational symmetry induced by the periodic boundary. The simulations were done with several magnetic field values with increasing field. The sample was also embedded in a vacuum layer to take the energy of the stray field into account. An example of the simulation result is shown in figure 24. The images show the absolute value and the phase of the order parameter with the case $\kappa = 0.5$ on left and $\kappa = 1.0$ on right. The topmost images are the thinnest case and the bottom images show the thickest. Two prominent features are immediately clear from the images: The fact that vortices are larger in the thinner case and that there are only singly quantized vortices in the case $\kappa = 1.0$ while the thick $\kappa = 0.5$ case shows giant vortices. Not all of the big vortices are giant vortices though. A pinning

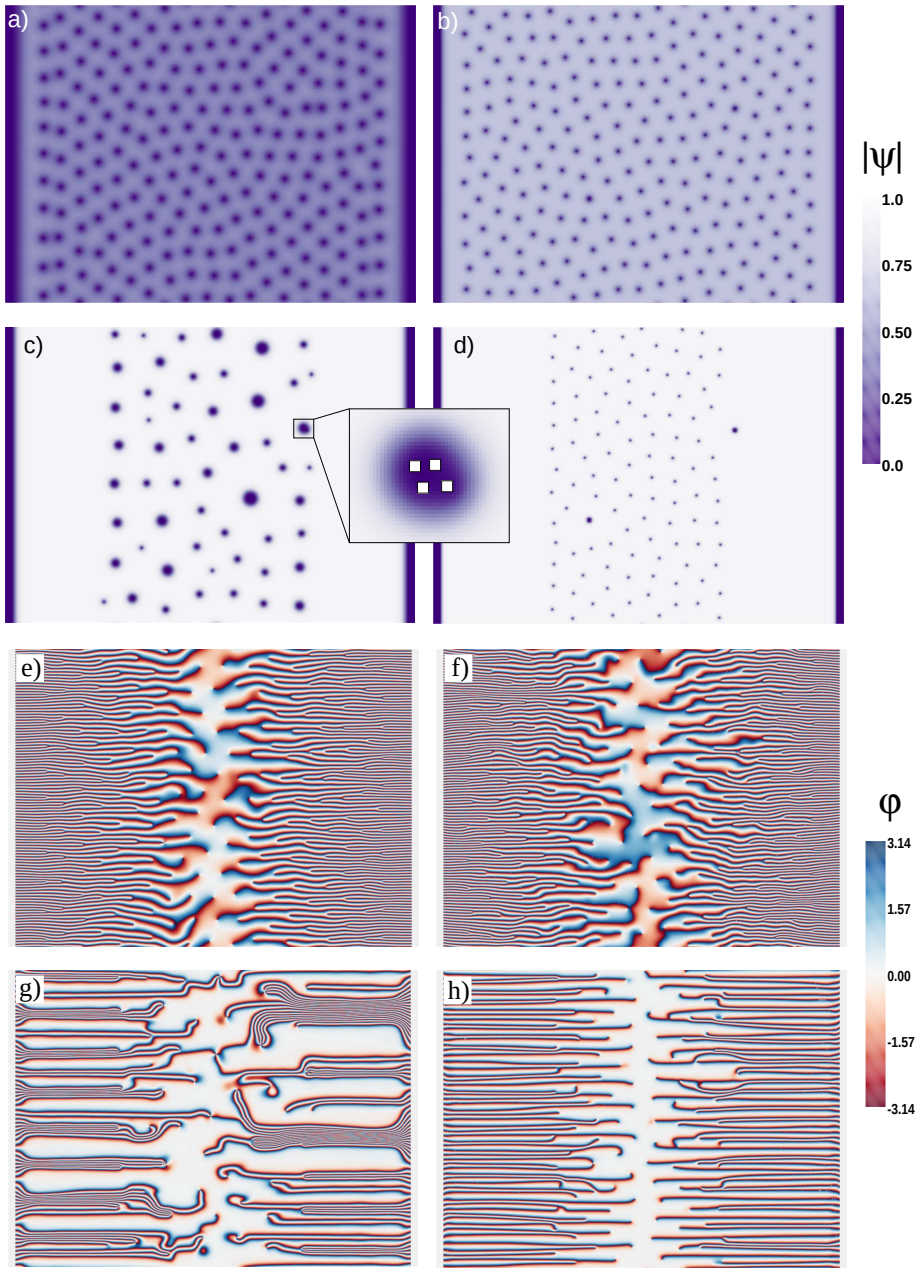

Figure 24. The absolute value (a-d) and the phase (e-h) of the order parameter shown on a plane cut through the centre of the sample perpendicular to the magnetic field. The simulation parameters used were (a, e) $\kappa = 0.5$ and $d = 3.5\xi_0$, (b, f) $\kappa = 1.0$ and $d = 3.5\xi_0$, (c, g) $\kappa = 0.5$ and $d = 15\xi_0$, (d, h) $\kappa = 1.0$ and $d = 15\xi_0$. The magnetic field is 0.5 mT. The size of the images is 37 µm × 27 µm (830 × 600 pixels). [**P5**]

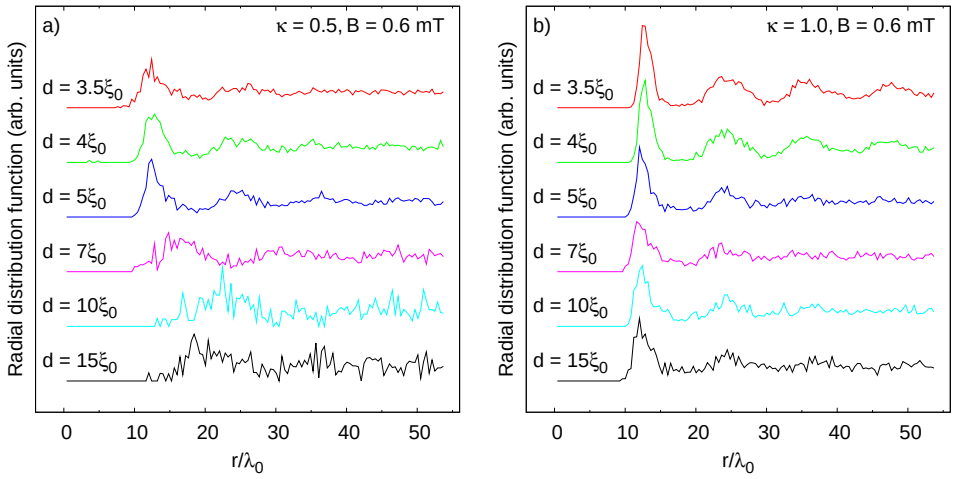

Figure 25. The radial distribution functions calculated from the vortex positions for the samples of different thicknesses with (a) $\kappa = 0.5$ and (b) $\kappa = 1.0$ at 0.6 mT. The given distances have been scaled with the bulk value of the penetration depth λ_0. [**P5**]

site seems to break down the symmetry of a giant vortex but the difference is very small. The estimated vortex core positions inside the multivortex are indicated with the white squares in the enlarged area of the image. Additionally, it can be seen how the different vortex-vortex interaction is reflected in the phase of the order parameter: The traces of the phase (a line of constant phase value) are packed closely together in the $\kappa = 0.5$ case showing the attractive interaction. In the $\kappa = 1.0$ case, the traces try to be as far away from each other as possible reflecting the repulsive nature of the vortices.

The radial distribution functions of the vortex positions in figure 25 show a lot more ordered vortex lattice in the $\kappa = 1.0$ case than in the type I case. For both values of κ the ordering of the vortex lattice increases with decreasing film thickness. In the type II case the nearest neighbour peak is at the same distance for all the thicknesses while for type I the peak shifts to larger distances. Naturally, the giant vortices have larger separation since there are several flux quanta in each. The peaks are also broader in the type I case indicating that the separation of the vortices is changing since the size (number of quanta) of the giant vortices is changing with film thickness.

The change in the size of the vortices with film thickness was determined by fitting the characteristic lengths ξ_{eff} and λ_{eff}. The fitting was done to the average profiles of the order parameter and magnetic field near the vacuum utilizing the analytic solutions to the Ginzburg-Landau equations in half space. The order parameter approaches zero

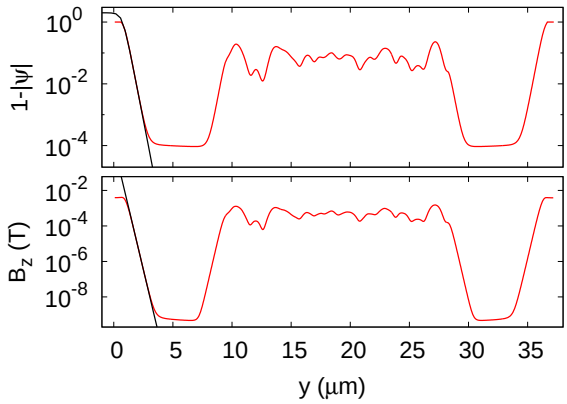

Figure 26. The average profile of the order parameter (top) and magnetic field (bottom). The fits of equations (34) and (35) to the profiles are shown as the black lines. The example shown here has been calculated from the case shown in figure 24(c) with simulation parameters of $\kappa = 0.5$, $d = 15\xi_0$ and $B = 0.5$ mT. [**P5**]

near the vacuum as [6]

$$\psi(y) = \tanh\left(\frac{y}{\sqrt{2}\xi_{\text{eff}}}\right), \tag{34}$$

where y is the distance to the surface of the superconductor and ξ_{eff} is the effective coherence length to be fitted with the function. In the same way, the behaviour of the magnetic field near the surface is exponential following [6]

$$B_z(y) = \exp\left(-\frac{y}{\lambda_{\text{eff}}}\right), \tag{35}$$

where λ_{eff} is the effective penetration depth to be fitted. Examples of fitting the effective lengths are given in figure 26 where the average profiles of the order parameter and the magnetic field through the sample are shown. There is a region near the surface where the fitting functions (34) and (35) agree with the profiles quite nicely.

The effective characteristic lengths both show the same thickness dependence that does not depend on the Ginzburg-Landau parameter when scaled with their bulk values ξ_0 and λ_0. The ξ_{eff} and λ_{eff} values are shown in figure 27 where the error bars show the deviation of the fit result for different values of the magnetic field. This universal behaviour has the form

$$\frac{X_{\text{eff}}}{X_0} = \frac{\xi_0}{d - d_0} + 1, \tag{36}$$

where $X = \lambda$ or ξ, and $d_0 \approx 3.3\xi_0$ obtained by the fits shown as the black lines in figure 27. In thin superconducting film the vortices take the form of Pearl vortices that

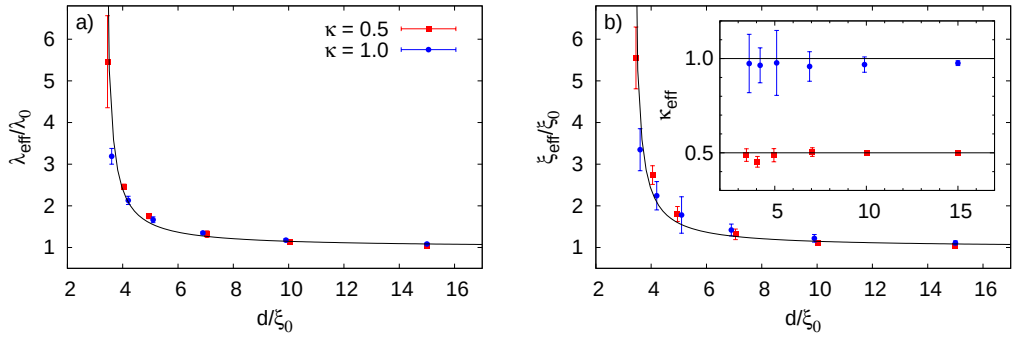

Figure 27. The effective penetration depth (a) and the coherence length (b) normalized with their bulk values as a function of the sample thickness. The inset shows the effective Ginzburg-Landau parameter as a function of the sample thickness. [**P5**]

have a long interaction length Λ, formulated by Pearl [100] as

$$\Lambda \sim \frac{\lambda_0^2}{d}. \tag{37}$$

Equation (36) can be rewritten as

$$\lambda_{\mathrm{eff}} = \frac{\lambda_0^2}{\kappa_0(d - d_0)} + \lambda_0, \tag{38}$$

where $\kappa_0 = \lambda_0/\xi_0$. Now the similarity between equations (37) and (38) is obvious. The prediction that the characteristic lengths increase with decreasing thickness is valid only up to the thickness where the mean free path of the electrons starts to restrict the coherence length since the mean free path effects are not included in the model.

It is interesting that the effective Ginzburg-Landau parameter, defined as

$$\kappa_{\mathrm{eff}} = \frac{\lambda_{\mathrm{eff}}}{\xi_{\mathrm{eff}}}, \tag{39}$$

shows no thickness dependence at all. It would seem logical that κ_{eff} increased with decreasing film thickness since the behaviour of the vortex lattice changes from type I to that resembling type II. Indeed, if the effective Ginzburg-Landau parameter is defined through the shear modulus of the vortex lattice κ_{eff} tends to infinity as the thickness decreases [101].

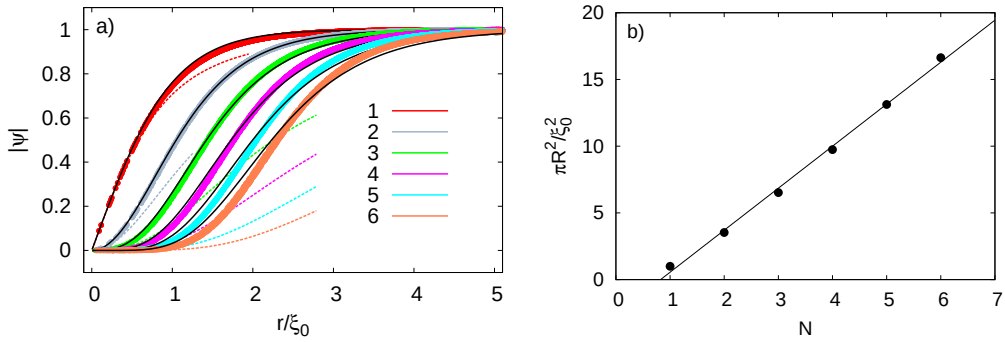

Figure 28. (a) The radial profiles of the cylindrically symmetric giant vortices of different number of flux quanta. The points are data from the simulation, the coloured dashed lines show equation (42) and the black solid lines show equation (43). (b) The area of the giant vortex core as a function of the number of flux quanta. The black line is a least squares fit to the data. Here, R is defined as $|\psi(r = R)| = 0.5$. **[P5]**

The radial profile of a singly quantized vortex can be estimated with the Clem model [102]

$$|\psi_1(r)| = \frac{r}{\sqrt{r^2 + \xi_0^2}}, \tag{40}$$

where r is the radial distance from the vortex core. An extension of the Clem model to the case of a giant vortex of N quanta was given by Lasher [103] as

$$\psi_N(r) = \left[\psi_1\left(\frac{r}{\sqrt{N}}\right)\right]^N, \tag{41}$$

which can with the Clem model be written as

$$\psi_N(r) = \left[\frac{r}{\sqrt{r^2 + N\xi_0^2}}\right]^N. \tag{42}$$

The radial profiles of giant vortices with different number of flux quanta are shown in figure 28 where the points show the profiles calculated from the simulation and the coloured dashed lines show the profile given by equation (42). The analytic expression for the profile given in equation (42) is based on the linearized Ginzburg-Landau equations which is a poor approximation in this case as can also be seen from its poor agreement with the simulation results.

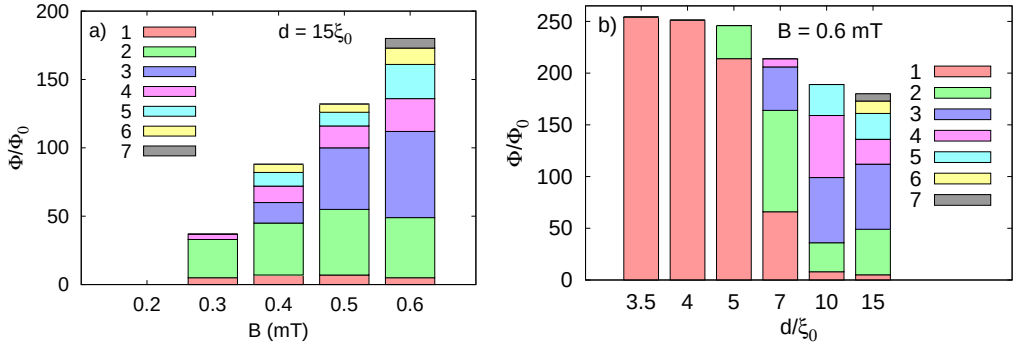

Figure 29. The distributions of the number of flux quanta in the giant vortices as a function of (a) magnetic field and (b) film thickness when $\kappa = 0.5$. The proportion of magnetic flux in different giant vortices is indicated by the colours. [**P5**]

In this case, a more practical analytic expression for fitting experimental data would be

$$\psi_N(r) = \left[\tanh\left(\frac{r}{N^{\frac{1}{4}}\xi_0}\right)\right]^N, \tag{43}$$

which is also shown as the black lines in figure 28(a). Equation (43) agrees quite well with the vortex profiles up to $N = 4$ after which some deviation starts to appear at higher values of N. The area of the vortex core increases linearly with the number of flux quanta as can be seen in figure 28(b) which is natural since the magnetic flux density is roughly constant inside the core. Thus, the area increases by the same amount for each quantum of flux. Here, the core of the vortex was defined as the area where $|\psi| < 0.5$.

In the case of $\kappa = 0.5$, the simulations show a continuous change from a lattice of singly quantized vortices into a mixed lattice of singly quantized and giant vortices of varying number of flux quanta. This is in contrast to the theoretical work of Lasher [104] who predicted that the giant vortices would form a honeycomb lattice consisting of identical giant vortices. The continuous change from the giant vortices to the singly quantized ones with film thickness is just a natural form of the intermediate state. But with the quirk that the energy minimum is such that the normal regions of the intermediate state consist of a single flux quantum due to the extreme thinness of the sample. Saying that a thin lead sample is type II superconductor is slightly misleading since the vortex state in it is a continuous extension of the intermediate state without any transition from type I to type II superconductivity.

The proportions of different giant vortices can be seen from the histogram in figure 29. The reason for the mixed lattice seems to be that the smaller vortices fill out the gaps between the larger vortices that are disturbed by the presence of the pinning sites. Indeed, the honeycomb structure of identical giant vortices could very well exist in the case, where there are no pinning sites breaking the ordering of the lattice. The presence of the singly quantized vortices at all thicknesses and magnetic field values in the $\kappa = 0.5$ case is interesting since it predicts that the singly quantized vortices are stable even in conditions that are close to bulk in type I superconductors. The stability has afterwards been confirmed by experiments where it was shown that annihilating a giant vortex with a giant antivortex of different number of flux quanta can result in a stable singly quantized vortex [97].

6 Conclusions

In this thesis, pulsed laser deposited YBCO thin films were seen to develop microcracks when grown on NGO or MgO substrates. The microcrack formation is connected to the structure of the YBCO film in both cases: with MgO the YBCO lattice rotates by 45° and with NGO the twin structure in the film is uniaxial. With NGO the parallel microcracks are very narrow and long while on MgO the cracks have two possible orientations and are wide and relatively short. The microcracks can be avoided by careful optimization of the deposition parameters and the film thickness.

Flux pinning caused by columnar nanorods was modelled by Ginzburg-Landau equations. The model fully includes all the vortex-vortex interactions and the non-linearity of the system. Thus, the measured magnetic field dependence of the critical current density was reproduced for BZO doped and undoped YBCO. The simulations showed that in addition to the large density also the large size of the BZO nanorods is a key factor behind the change in the power law behaviour between BZO doped and undoped YBCO. In addition to the lower α value, the characteristic shape of the magnetic field dependence was also heavily modified by the BZO nanorods. The large size of the columnar pinning sites was also seen to strongly suppress the long range order of the vortex lattice.

The Ginzburg-Landau equations were solved for type I thin films where giant vortices were seen to appear depending on the film thickness. The simulations predicted that singly quantized vortices are stable in type I films up to quite large thicknesses and recent experimental results give support to this prediction [97]. Pinning sites were seen to break the giant vortices into multivortices. The size of the vortices increased with decreasing film thickness in a way that is similar to the behaviour of the interaction length of Pearl vortices.

The upper critical field measurements revealed that the BZO nanorods decrease the effective electron mass anisotropy of YBCO from $\gamma = 6.0$ in the undoped case to $\gamma = 3.4$ in the 5 wt-% BZO doped case. Even though the anisotropy was modified, the shape of the angular dependence of the upper critical field remained in the form given by the Blatter scaling in all cases. The angular dependence of the irreversibility field could not be explained with the Blatter scaling in any of the cases. In conclusion, the effective electron mass anisotropy of YBCO cannot be measured from the critical current density nor from the irreversibility field which are determined by the pinning landscape of the material.

References

[1] H. Onnes, Leiden Comm. **120b, 122b, 124c**, (1911).

[2] L. N. Cooper, Phys. Rev. **104**, 1189 (1956).

[3] J. Bardeen, L. N. Cooper, and J. R. Schrieffer, Phys. Rev. **108**, 1175 (1957).

[4] F. Duan and J. Guojun, *Introduction to Condensed Matter Physics, Volume 1* (World Scientific Publishing, 2005).

[5] V. L. Ginzburg and L. D. Landau, Zh. Eksp. Teor. Fiz. **20**, 1064 (1950).

[6] C. P. Poole Jr., H. A. Farach, R. J. Creswick, and R. Prozorov, *Superconductivity, Second Edition* (Academic Press, 2007).

[7] A. A. Abrikosov, Soviet Physics JETP **5**, 1174 (1957).

[8] T. P. Orlando and K. A. Delin, *Foundations of Applied Superconductivity* (Addison-Wesley, 1991).

[9] U. Essmann and H. Träuble, Phys. Lett. A **24**, 526 (1967).

[10] G. Blatter, V. B. Geshkenbein, and J. A. G. Koopmann, Phys. Rev. Lett. **92**, 067009 (2004).

[11] G. Blatter *et al.*, Reviews of Modern Physics **66**, 1125 (1994).

[12] E. Mezzetti *et al.*, Phys. Rev. B **60**, 7623 (1999).

[13] C. Cai *et al.*, Phys. Rev. B **69**, 104531 (2004).

[14] P. Paturi, M. Irjala, H. Huhtinen, and A. B. Abrahamsen, J. Appl. Phys. **105**, 023904 (2009).

[15] C. J. van der Beek *et al.*, Phys. Rev. B **66**, 24523 (2002).

[16] M. K. Wu *et al.*, Phys. Rev. Lett. **58**, 908 (1987).

[17] J. G. Bednorz and K. A. Müller, Z. Phys. B **64**, 189 (1986).

[18] J. G. Ossandon *et al.*, Phys. Rev. B **45**, 12534 (1992).

[19] J. D. Jorgensen *et al.*, Phys. Rev. B **41**, 1863 (1990).

[20] J. Zaanen, A. T. Paxton, O. Jepsen, and O. K. Andersen, Phys. Rev. Lett. **60**, 2685 (1988).

[21] A. Latgé, E. V. Anda, and J. L. Morán-Lopéz, Phys. Rev. B **42**, 4288 (1990).

[22] U. Welp *et al.*, Phys. Rev. Lett. **62**, 1908 (1989).

[23] D. R. Harshman *et al.*, Phys. Rev. B **39**, 851 (1989).

[24] L. Krusin-Elbaum *et al.*, Phys. Rev. B **39**, 2936 (1989).

[25] S. N. Song *et al.*, Appl. Phys. Lett. **51**, 1376 (1987).

[26] T. R. Dinger, T. K. Worthington, W. J. Gallagher, and R. L. Sandstrom, Phys. Rev. Lett. **58**, 2687 (1987).

[27] W. J. Gallagher, J. Appl. Phys. **63**, 4216 (1988).

[28] K. Nakao *et al.*, Phys. Rev. Lett. **63**, 97 (1989).

[29] G. Blatter, V. B. Geshkenbein, and A. I. Larkin, Phys. Rev. Lett. **68**, 875 (1992).

[30] P. Paturi, M. Irjala, and H. Huhtinen, J. Appl. Phys. **103**, 123907 (2008).

[31] J. Gutiérrez *et al.*, Nat. Mater. **6**, 367 (2007).

[32] L. Civale *et al.*, Appl. Phys. Lett. **84**, 2121 (2004).

[33] S. Wimbush and N. Long, New J. Phys. **14**, 083017 (2012).

[34] B. Maiorov *et al.*, Supercond. Sci. Technol. **20**, S223 (2007).

[35] P. J. M. van Bentum *et al.*, Physica B **155**, 160 (1989).

[36] R. J. Wijngaarden *et al.*, Physica C **152**, 523 (1988).

[37] T. K. Worthington, W. J. Gallagher, and T. R. Dinger, Phys. Rev. Lett. **59**, 1160 (1987).

[38] S. R. Foltyn *et al.*, Nat. Mater. **6**, 631 (2007).

[39] L. Civale *et al.*, Phys. Rev. Lett. **65**, 1164 (1990).

[40] L. Civale *et al.*, Phys. Rev. Lett. **67**, 648 (1991).

[41] B. Roas, B. Hensel, G. Saemann-Ischenko, and L. Schultz, Appl. Phys. Lett. **54**, 1051 (1989).

[42] J. L. MacManus-Driscoll *et al.*, Nat. Mater. **3**, 439 (2004).

[43] C. V. Varanasi *et al.*, Supercond. Sci. Technol. **19**, L37 (2006).

[44] C. V. Varanasi *et al.*, J. Appl. Phys. **102**, 063909 (2007).

[45] B. Maiorov *et al.*, Nat. Mater. **8**, 398 (2009).

[46] V. F. Solovyov *et al.*, Supercond. Sci. Technol. **20**, L20 (2007).

[47] M. Peurla *et al.*, Supercond. Sci. Technol. **19**, 767 (2006).

[48] M. Malmivirta *et al.*, Thin Solid Films (submitted) .

[49] R. Wördenweber, Supercond. Sci. Technol. **12**, R86 (1999).

[50] J. Raittila, H. Huhtinen, P. Paturi, and Y. P. Stepanov, Physica C **371**, 90 (2002).

[51] R. M. Hazen, Am. Mineral. **61**, 266 (1976).

[52] V. G. Tsirelson *et al.*, Acta Crystallogr. Sect. B **54**, 8 (1998).

[53] W. Marti *et al.*, J. Phys.: Condens. Matter **6**, 127 (1994).

[54] S. B. Ubizskii *et al.*, Supercond. Sci. Technol. **7**, 766 (1994).

[55] R. J. Angel *et al.*, J. Solid State Chem. **180**, 3408 (2007).

[56] Y. A. Abramov *et al.*, Acta Crystallogr. Sect. B **51**, 942 (1995).

[57] T. Yamanaka, N. Hirai, and Y. Komatsu, Am. Mineral. **87**, 1183 (2002).

[58] B. D. Cullity, *Elements of X-ray diffraction, 2nd ed.* (Addison-Wesley Publishing Company Inc., 1978).

[59] H. P. Wiesinger, F. M. Sauerzopf, and H. W. Weber, Physica C **203**, 121 (1992).

[60] J. Jäykkä, J. Hietarinta, and P. Salo, Phys. Rev. B **77**, 094509 (2008).

[61] C. G. Broyden, J. Inst. Math. Appl. **6**, 76 (1970).

[62] R. Fletcher, Comput. J. **13**, 317 (1970).

[63] D. Goldfarb, Math. Comput. **24**, 23 (1970).

[64] D. F. Shanno, Math. Comput. **24**, 647 (1970).

[65] J. Nam *et al.*, J. Appl. Phys. **97**, 123906 (2005).

[66] G. Koren *et al.*, Appl. Phys. Lett. **73**, 3763 (1998).

[67] H. Huhtinen *et al.*, IEEE Trans. Appl. Supercond. **13**, 2777 (2003).

[68] T. Venkatesan *et al.*, Appl. Phys. Lett. **54**, 581 (1989).

[69] M. Peurla *et al.*, IEEE Trans. Appl. Supercond. **17**, 3608 (2007).

[70] Y. Yamada *et al.*, Jpn. J. Appl. Phys. **39**, 1111 (2000).

[71] J. L. MacManus-Driscoll, J. C. Bravman, and R. B. Beyers, Physica C **241**, 401 (1995).

[72] M. Mukaida *et al.*, Supercond. Sci. Technol. **17**, 337 (2004).

[73] A. Kulpa *et al.*, Supercond. Sci. Technol. **3**, 483 (1990).

[74] O. Chaix-Pluchery, B. Chenevier, and J. J. Robles, Appl. Phys. Lett. **86**, 251911 (2005).

[75] V. Pan *et al.*, Phys. Rev. B **73**, 054508 (2006).

[76] P. Paturi, Supercond. Sci. Technol. **23**, 025030 (2010).

[77] N. J. Long, N. M. Strickland, and E. F. Talantsev, IEEE Trans. Appl. Supercond. **17**, 3684 (2007).

[78] N. J. Long, Supercond. Sci. Technol. **21**, 025007 (2008).

[79] A. Augieri *et al.*, J. Appl. Phys. **108**, 063906 (2010).

[80] V. Svetchnikov, V. Pan, C. Træholt, and H. Zandbergen, IEEE Trans. Appl. Supercond. **7**, 1396 (1997).

[81] B. Dam *et al.*, Nature **399**, 439 (1999).

[82] M. Peurla, H. Huhtinen, and P. Paturi, Supercond. Sci. Technol. **18**, 628 (2005).

[83] H. Huhtinen *et al.*, IEEE Trans. Appl. Supercond. **17**, 3620 (2007).

[84] H. Huhtinen, K. Schlesier, and P. Paturi, Supercond. Sci. Technol. **22**, 075019 (2009).

[85] H. Huhtinen, M. Irjala, P. Paturi, and M. Falter, IEEE Trans. Appl. Supercond. **21**, 2753 (2011).

[86] A. Bezryadin, Y. N. Ovchinnikov, and B. Pannetier, Phys. Rev. B **53**, 8553 (1996).

[87] M. Peurla *et al.*, Phys. Rev. B **75**, 184524 (2007).

[88] A. Llordés *et al.*, Nat. Mater. **11**, 329 (2012).

[89] T. Matsushita *et al.*, Supercond. Sci. Technol. **25**, 125003 (2012).

[90] M. Miura *et al.*, Appl. Phys. Lett. **96**, 072506 (2010).

[91] S. A. Baily *et al.*, Phys. Rev. Lett. **100**, 027004 (2008).

[92] S. Hasegawa *et al.*, Phys. Rev. B **43**, 7631 (1991).

[93] T. Cren, L. Serrier-Garcia, F. Debontridder, and D. Roditchev, Phys. Rev. Lett. **107**, 097202 (2011).

[94] M. A. Engbarth, S. J. Bending, and M. V. Milošević, Phys. Rev. B **83**, 224504 (2011).

[95] A. V. Silhanek *et al.*, Phys. Rev. B **83**, 024509 (2011).

[96] R. B. G. Kramer *et al.*, Physica C **470**, 758 (2010).

[97] J. Ge, J. Gutierrez, J. Cuppens, and V. V. Moshchalkov, Phys. Rev. B **88**, 174503 (2013).

[98] M. Tinkham, Phys. Rev. **129**, 2413 (1963).

[99] K. Maki, Ann. Phys. **34**, 363 (1965).

[100] J. Pearl, Appl. Phys. Lett. **5**, 65 (1964).

[101] E. H. Brandt, Phys. Rev. B **71**, 014521 (2005).

[102] J. R. Clem, J. Low Temp. Phys. **18**, 427 (1975).

[103] G. Lasher, Phys. Rev. **140**, A523 (1965).

[104] G. Lasher, Phys. Rev. **154**, 345 (1967).